AGU PUBLICATIONS

JGR

Journal of Geophysical Research: Oceans

RESEARCH ARTICLE

10.1002/2014JC010487

Passive buoyant tracers in the ocean surface boundary layer: 1. Influence of equilibrium wind-waves on vertical distributions

T. Kukulka[1] and K. Brunner[1]

[1]School of Marine Science and Policy, College of Earth, Ocean, and Environment, University of Delaware, Newark, Delaware, USA

Key Points:
- Langmuir (and not breaking wave) turbulence deeply submerges buoyant tracers
- For young seas, breaking waves critically enhance near-surface mixing
- Stokes drift decay length is a key for parameterizing wave-driven turbulence

Correspondence to:
T. Kukulka,
kukulka@udel.edu

Citation:
Kukulka, T., and K. Brunner (2015), Passive buoyant tracers in the ocean surface boundary layer: 1. Influence of equilibrium wind-waves on vertical distributions, *J. Geophys. Res. Oceans*, *120*, doi:10.1002/2014JC010487.

Received 17 OCT 2014
Accepted 6 MAY 2015
Accepted article online 9 MAY 2015

Abstract This paper is the first of a two part series that investigates passive buoyant tracers in the ocean surface boundary layer. The first part examines the influence of equilibrium wind-waves on vertical tracer distributions, based on large eddy simulations (LES) of the wave-averaged Navier-Stokes equation. The second part applies the model to investigate observations of buoyant microplastic marine debris, which has emerged as a major ocean pollutant. The LES model captures both Langmuir turbulence (LT) and enhanced turbulent kinetic energy input due to breaking waves (BW) by imposing equilibrium wind-wave statistics for a range of wind and wave conditions. Concentration profiles of LES agree well with analytic solutions obtained for an eddy diffusivity profile that is constant near the surface and transitions into the K-Profile Parameterization (KPP) profile shape at greater depth. For a range of wind and wave conditions, the eddy diffusivity normalized by the product of water-side friction velocity and mixed layer depth, h, mainly depends on a single nondimensional parameter, the peak wavelength (which is related to Stokes drift decay depth) normalized by h. For smaller wave ages, BW critically enhances near-surface mixing, while LT effects are relatively small. For greater wave ages, both BW and LT contribute to elevated near-surface mixing, and LT significantly increases turbulent transport at greater depth. We identify a range of realistic wind and wave conditions for which only Langmuir (and not BW or shear driven) turbulence is capable of deeply submerging buoyant tracers.

1. Introduction

This study is the first of a two part series that investigates passive buoyant tracers in the ocean surface boundary layer (OSBL). The first part models the influence of idealized equilibrium wind-wave conditions on vertical tracer distributions. The second part applies the model to investigate observations of buoyant microplastic marine debris, which is now recognized as one of the major ocean pollutants [*Law et al*., 2010, 2014].

Buoyant tracers in the ocean surface boundary layer play a key role in a myriad of physical, biological, geological, chemical, and environmental processes. Upper ocean turbulence distributes buoyant tracers, such as plankton [*Denman and Gargett*, 1995], bubbles [*Thorpe*, 1982; *Liang et al*., 2011; *Gemmrich*, 2012], and pollutants [*D'Asaro*, 2000; *Kukulka et al*., 2012b; *Yang et al*., 2014]. In particular, observations and a one-dimensional column model indicate that microplastic marine debris is vertically distributed within the upper water column due to wind-driven mixing [*Kukulka et al*., 2012b]. This paper is aimed at systematically exploring the enhanced OSBL mixing due to surface gravity waves for idealized ocean and buoyant tracer conditions.

Nonbreaking ocean surface waves influence upper ocean turbulence because greater below-crest and smaller below-trough wave orbital speeds induce a residual flow (Stokes drift) that tilts vertical vorticity into the direction of wave propagation [*Craik and Leibovich*, 1976]. This vortex tilting interacts with sheared surface currents to form wind-aligned roll vortices, called Langmuir circulation [*Langmuir*, 1938] or Langmuir turbulence (LT), recognizing its turbulence characteristics [*McWilliams et al*., 1997; *Grant and Belcher*, 2009]. LT is captured by the Craik-Leibovich vortex force that results from wave averaging of the Navier-Stokes equation [*Leibovich*, 1983]. State-of-the-art LT models are commonly based on turbulence-resolving large eddy simulations (LES) adopting the systematic mathematical theory by *Craik and Leibovich* [1976] [*Skyllingstad and Denbo*, 1995; *McWilliams et al*., 1997; *Li et al*., 2005]. LES model results have been successfully

compared to observations [*Skyllingstad et al*., 1999; *Gargett et al*., 2004; *Li et al*., 2009; *Kukulka et al*., 2009, 2011; *Harcourt and D'Asaro*, 2010]. Buoyant tracers in an LES context have been addressed previously [e.g., *Colbo and Li*, 1999; *Skyllingstad*, 2003; *Harcourt and D'Asaro*, 2010; *Liang et al*., 2011]; however, only *Liang et al*. [2011] have considered explicitly enhanced near-surface mixing in the presence of a breaking wave field.

Breaking ocean surface waves transfer some of their energy to subsurface turbulent kinetic energy (TKE) [*Craig and Banner*, 1994; *Terray et al*., 1996; *Melville*, 1996]. The resulting enhanced turbulence intensities and dissipation rates, in turn, are expected to contribute significantly in mixing close to the surface. Breaking waves (BWs) have been parameterized in an LES with LT effect by a random surface forcing to imitate TKE injection by BW [*Noh et al*., 2004; *Li et al*., 2013]. Such an approach does not capture local space-time dynamics of breakers, which have been modeled in a direct numerical simulation without LT [*Sullivan et al*., 2004]. A similar BW approach was incorporated in an LES with LT to depict realistically the interaction between LT and BWs [*Sullivan et al*., 2007]. This LES model has been applied to investigate the evolution of polydisperse bubble distributions [*Liang et al*., 2011]. Breaking wave effects are mainly confined to a relatively thin (compared to the total mixed layer depth) near-surface layer, whose depth scales with significant wave height H_s [*Terray et al*., 1996]. In spite of the recent progress in modeling BW effects, important open questions remain related to the dynamics of individual BW events and their oceanic distributions [e.g., *Melville and Matusov*, 2002; *Melville et al*., 2002; *Gemmrich et al*., 2008; *Kukulka and Hara*, 2008a, 2008b]. Given the incomplete state of knowledge, our goal is to implement a simple wave breaking scheme that is energetically constrained and captures the enhanced near-surface mixing that is expected to play a key role for the vertical distributions of buoyant tracers.

As a first step, we will examine the vertical distributions of buoyant tracer concentrations in idealized wind and wave conditions and address the following questions. Under what wind and wave conditions are buoyant tracers deeply submerged? What are the key parameters that determine the vertical tracer distributions? What is the role of breaking waves and Langmuir turbulence in the submergence processes? How effective is a simple analytic model to describe enhanced wave mixing effects?

In the next section, we consider a simple analytic model that provides valuable conceptual insights and serves as a basis for a practical parametric model. The key unknown in determining the vertical distribution of buoyant tracers is the advective transport by wave-driven turbulence, which is, therefore, investigated in detail. Section 3 describes the turbulence-resolving LES model that includes wave breaking and Langmuir turbulence effects for equilibrium wind-waves. LES model results are discussed and interpreted in light of the analytic model in section 4, before concluding the paper with section 5.

2. Analytic Considerations

As a first step to investigate passive buoyant tracers, we consider the tracer as buoyant particles and assume that their velocity is given by the sum of fluid velocity and constant buoyant rise velocity $w_b > 0$. This assumption holds if (a) the particle inertial relaxation time scale is small relative to the turbulent time scale (equivalent to a small Stokes number) and (b) the only forces on the particle are due to friction and gravity [see, e.g., *Guha*, 2008; *Veron*, 2015]. With this assumption, the Reynolds-averaged transport equation for a buoyant tracer at concentration $\tilde{C} = \langle \tilde{C} \rangle + \tilde{C}'$ in stationary and horizontally homogeneous conditions is

$$w_b C + \langle w' \tilde{C}' \rangle = 0, \tag{1}$$

where angle brackets indicate horizontally averaged quantities, primed variables are the deviation from such averages, $C = \langle \tilde{C} \rangle$, and w is the vertical fluid velocity, $\langle w' \tilde{C}' \rangle$ is the vertical turbulent tracer flux. The turbulent flux is parameterized via an eddy mixing coefficient $A(z)$

$$\langle w' \tilde{C}' \rangle = -A(z) \frac{dC}{dz}, \tag{2}$$

where z is the vertical coordinate increasing upward. This parameterization is straightforward and effective for our application, but neglects nonlocal turbulent flux terms [*Large et al*., 1994]. Nonlocal turbulent fluxes may play an important role in LT, but are currently not well understood [*Smyth et al*., 2002; *McWilliams et al*.,

2012]. As a first step, we assume that $A(z)$ does not explicitly depend on w_b, which is consistent with previous simple turbulent diffusion models of buoyant tracers [e.g., *Thorpe*, 1982] and effective for our study. This assumptions is not made for the LES approach and its in-depth assessment for the Reynolds-averaged approach is left for future work (see also discussions by *Thorpe et al.* [2003] and *Veron* [2015]). Thus, scaled analytic solutions are self-similar and depend only on $A(z)$

$$\left(\frac{C(z)}{C(0)}\right)^{1/w_b} = \exp\left(\int_z^0 -\frac{1}{A(\zeta)}d\zeta\right). \tag{3}$$

Clearly, w_b and $A(z)$ are key parameters for vertical tracer concentration distributions. To model the vertical distribution of buoyant tracers, we need to investigate in detail the unknown eddy diffusivity coefficient due to wave-driven turbulence. Once A is determined, C can be readily computed for different w_b.

2.1. Near-Surface Mixing

Let the mixing coefficient near the surface be $A(0) = A_0$. For small $|z|$ with $|z| \ll A(dA/dz)^{-1}$, the approximate solution (3) is

$$C(z) = C(0)\exp\left(\frac{w_b}{A_0}z\right). \tag{4}$$

The decay length scale of the C profile

$$d = A_0/w_b, \tag{5}$$

approaches zero as A_0 goes to zero for fixed w_b. Therefore, buoyant material is effectively surface trapped for small near-surface mixing. In this case, the surface concentration is inversely proportional to A_0 for a given total concentration. For deep submergence, d must be large enough to overcome this surface trapping (lines with circles in Figure 1 with $d = 0.15$, 0.5, and 1.5 m (black, blue, and red, respectively)).

2.2. Solid-Wall Boundary Layer Turbulence

Assume $A(z) = A_0 = \kappa z_0 u_*$ is constant near the surface and transitions to its estimate for a shear-driven solid-wall turbulent boundary layer below depth z_0, so that the eddy diffusivity is

$$A(z) = \kappa|z|u_*, \tag{6}$$

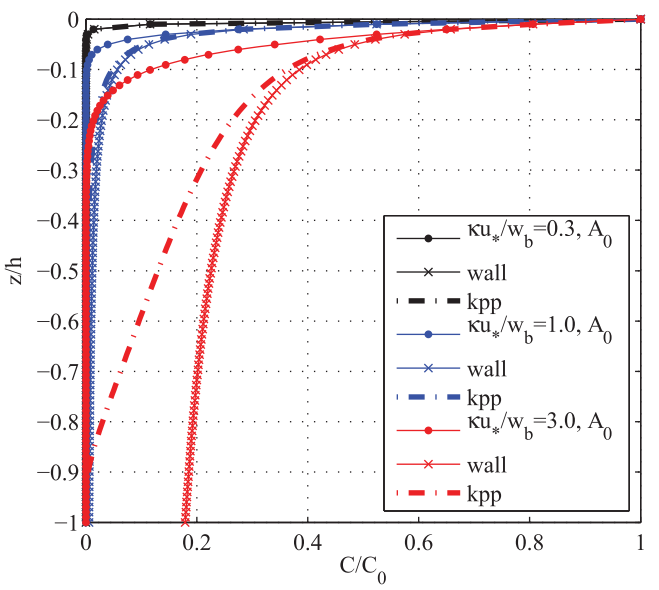

Figure 1. Analytic buoyant tracer profile solutions for constant A solution (4) (line with circles), solid wall boundary layer solution (7) (line with crosses), and the KPP solution (9) (dash-dotteded line) for different $\kappa u_*/w_b = 0.3$ (black), 1.0 (blue), 3.0 (red), corresponding to $w_b \approx 1.1, 0.3, 0.1$ cm/s, or $d = 0.15$, 0.5, 1.5 m, respectively. Solutions were obtained for $u_* = 0.85$ cm/s and $z_0 = 0.5$ m.

for $|z| > z_0$. Here $\kappa = 0.4$ is the von Karman constant, u_* is the water-side friction velocity, and z_0 denotes a hydrodynamic roughness length z_0 [*Craig and Banner*, 1994]. The analytic solution for $|z| \le z_0$ is given by (4) and the solution for $|z| > z_0$ is

$$C(z) = C(0)\exp\left(-\frac{w_b}{\kappa u_*}\right)\left(\frac{|z|}{z_0}\right)^{-\frac{w_b}{\kappa u_*}}. \tag{7}$$

Solutions illustrate that buoyant material is deeply submerged for $d \gg z_0$ or equivalently $\kappa u_*/w_b \gg 1$ with more vertically homogenous distributions for larger $\kappa u_*/w_b$ (lines with crosses in Figure 1). If the tracer is deeply submerged and the condition $(z_0/h)^{\frac{w_b}{\kappa u_*}} \ll 1$ is not satisfied, the tracer will significantly penetrate into the bottom boundary layer. Here h is a depth scale for the upper ocean boundary layer.

2.3. KPP Closure Solutions

If the tracer extends into depths close to $z = -h$, the whole profile of $A(z)$ in the boundary layer needs to be specified. We apply a common upper ocean boundary layer model based on K (eddy diffusivity) Profile Parameterizations (KPP) [*Large et al.*, 1994]. Key parameters in the KPP model are a velocity scale w_* and the boundary layer depth h. If $z_T > 0$ is the transition depth from constant A_0, the eddy diffusivity for $|z| > z_T$ is specified by

$$A(z) = -w_* h \left(\frac{z}{h}\right)\left(1+\frac{z}{h}\right)^2. \tag{8}$$

For a neutrally stratified solid wall boundary layer, $w_* = \kappa u_*$, so that $A(z) \to \kappa|z|u_*$ close to the surface. Furthermore, note that $z_T \approx A_0/w_*$. Assuming w_* is constant with depth, the analytic solution for $|z| > z_T$ is

$$C(z) = C(z_T)\left(\frac{h+z}{z_T-h}\frac{z_T}{z}\right)^{\frac{w_b}{w_*}} \exp\left(\frac{w_b}{w_*}\frac{z_T+z}{h+z}\frac{h}{h-z_T}\right). \tag{9}$$

The C profile becomes more uniform for smaller w_b/w_* (dash-dotted lines in Figure 1, where $w_* = \kappa u_*$).

The length scale h in the KPP model is fixed at $h = c_h 35$ m for all model runs, where 35 m is the typical mixed layer depth (see below) and c_h denotes a constant empirical coefficient $c_h = 8/7$. This modification assures that the C profile for deep submergence approaches zero for $z \to -h$, rather than for $z \to -h/c_h$ (see Figure 1 for model results without c_h). This coefficient influences only weakly near-surface mixing ($A \to w_* z$ for $z \to 0$), which is the focus of this study. However, model results suggest that this modification captures more accurately mixing at the mixed layer base (note that $A(-h) = 0$ according to (8)).

2.4. Wave Effects

Wave enhanced mixing contributes to deep submergence in complex ways. Waves may enhance near-surface mixing, which is parameterized by A_0. Breaking waves inject turbulent kinetic energy (TKE) to increase mixing rates [*Craig and Banner*, 1994]. Langmuir turbulence, on the other hand, sets up small-scale coherent motion that elevates transport [*Veron and Melville*, 2001]. Potentially, stochastic energetic BW disrupts organized LT motion [*McWilliams et al.*, 2012] or BWs seed vertical vorticity to drive LT [*Sullivan et al.*, 2007], so that both near-surface wave effects generally interact. Furthermore, large-scale Langmuir circulations enhance deep transport due to coherent motions that extend throughout the mixed layer.

Both wave effects are parameterized here with two enhancement factors relative to solid wall boundary layer turbulence c_0 for near surface and c_w for deep mixing by letting

$$A_0 = c_0 \kappa z_0 u_*, \tag{10}$$

$$w_* = c_w \kappa u_*. \tag{11}$$

The enhancement factor c_w was first introduced by *McWilliams and Sullivan* [2000], who showed its dependence on turbulent Langmuir number $La_t = \sqrt{u_*/u_{s0}}$, where u_{s0} is the surface Stokes drift.

The wave enhancement factors c_0 and c_w will be systematically determined based on a rational model for wave-driven upper ocean turbulence for a range of realistic environmental conditions. One advantage of determining A from stationary buoyant tracer solutions is that the mean buoyant upward flux is balanced by the turbulent downward flux, so that eddy diffusivity coefficients are readily determined from robust mean concentrations, rather than eddy covariances.

3. LES With Wave Effects

3.1. Basic Model

Following *McWilliams et al.* [1997] with the modifications proposed by *Kukulka et al.* [2010, 2012a], the subgrid-scale (SGS) filtered velocity field is obtained by

$$\frac{\partial \bar{u}_i}{\partial t}+\bar{u}_j\frac{\partial \bar{u}_i}{\partial x_j}+\epsilon_{ikm}f_k(\bar{u}_m+u_{s,m})= -\frac{\partial \bar{\pi}}{\partial x_i}+\frac{\bar{\rho}}{\rho_0}g_i+\epsilon_{ikm}u_{s,k}\bar{\omega}_m-\frac{\partial \tau_{ij}^{SGS}}{\partial x_j}, \tag{12}$$

where t denotes time, u_i is the three-dimensional velocity, $(f_1, f_2, f_3)=(0, 0, f)$ is the planetary vorticity with Coriolis parameter f, $u_{s,k}$ is the Stokes drift vector along the wind direction $x_1 = x$, π is a generalized pressure, ρ is the density, ρ_0 denotes a constant reference density, ω_i is vorticity, and $(g_1, g_2, g_3)=(0, 0, -g)$ is the gravitational acceleration. The bars indicate SGS filtered quantities. Turbulent SGS fluxes are parameterized via an SGS eddy viscosity,

$$\tau_{ij}^{SGS}=-K_M\left(\frac{\partial \bar{u}_i}{\partial x_j}+\frac{\partial \bar{u}_j}{\partial x_i}\right), \tag{13}$$

which is expressed as $K_M=le^{1/2}$ and depends on the SGS TKE, e, and an SGS length scale, l, determined by the spatial resolution, $l=\Delta s=(\Delta x\Delta y\Delta z)^{1/3}$ if stratification is zero or negative and l is damped if stratification is positive (see *Moeng* [1984] for details). Here Δx, Δy, and Δz denotes the grid resolution in x, y, and z, respectively. The SGS TKE, in turn, is determined from the prognostic equation

$$\frac{\partial e}{\partial t}+\bar{u}_j\frac{\partial e}{\partial x_j}=\tau_{ij}^{SGS}\frac{\partial \bar{u}_i}{\partial x_j}+g\rho_0^{-1}\tau_{\rho}^{SGS}+\frac{\partial}{\partial x_i}\left(2K_M\frac{\partial e}{\partial x_i}\right)-\epsilon, \tag{14}$$

where τ_{ρ}^{SGS} is the SGS density flux and the turbulent dissipation rate ϵ is $\epsilon=Be^{3/2}/l$ with $B=0.19+0.51l(\Delta x\Delta y\Delta z)^{-1/3}$. Note that (14) could include a SGS Stokes drift shear production term $\tau_{ij}^{SGS}\frac{\partial u_{s,i}}{\partial x_j}$ [*McWilliams et al.*, 1997]. However, our LES results are not sensitive to the inclusion of this production term because without breaking waves the LES is well resolved and not sensitive to the SGS scheme (breaking waves dominate SGS TKE input if they are included). The transport equation for a buoyant tracer θ is

$$\frac{\partial \bar{\theta}}{\partial t}+(u_{s,j}+\bar{u}_j+w_b\delta_{j3})\frac{\partial \bar{\theta}}{\partial x_j}=-\frac{\partial \tau_{\theta j}^{SGS}}{\partial x_j}, \tag{15}$$

where the subgrid-scale θ flux $\tau_{\theta j}^{SGS}$ is parameterized as

$$\tau_{\theta j}^{SGS}=-K_{\theta}\frac{\partial \bar{\theta}}{\partial x_j}, \tag{16}$$

with $K_{\theta}=[1+(2l/\Delta s)]K_M$.

Our default LES domain has horizontal dimensions of $x_l = y_l = 150$ m and a total depth of $z_l = 90$ m with $128 \times 128 \times 300$ grid points, which captures most of the energy and flux carrying eddies. The Coriolis parameter is $f = 10^{-4}$ s^{-1}. The initial temperature profile is constant the first 32 m followed by a temperature gradient of 0.02 K/m. Small buoyancy entrainment typically results in $h \approx 35$ m during the course of the numerical experiments. Fields are spun-up sufficiently to be fully turbulent and then sampled to obtain robust mean tracer statistics, which are quasi-stationary and only weakly dependent on the phase of the inertial current.

Note that for sufficiently small u_*/w_b, buoyant tracer distributions are strongly influenced by small-scale turbulence close to the air-sea interface, which our LES does not resolve. In this case, subgrid-scale processes dominate overresolved ones and the LES model performs similarly to a Reynolds-averaged Navier-Stokes equation (RANS) approach for the buoyant tracer. Resolving all near-surface motion down to the dissipative scale, however, is computationally much more expensive for the high Reynolds number flow under consideration [*Pope*, 2008]. Such an approach also requires additional knowledge of the short-wave spectrum, breaking wave distribution, and phase-resolved wave dynamics. These are important open research questions beyond the scope of this paper. The strength of our approach is that it relies on rational models of LT and BW that are constrained by momentum and energy conservation.

3.2. Wave Spectrum and Stokes Drift

Our approach to implementing the Stokes drift profile for equilibrium wind-driven seas is consistent with the work by *Harcourt and D'Asaro* [2008], who have also thoroughly reviewed its strengths and limitations.

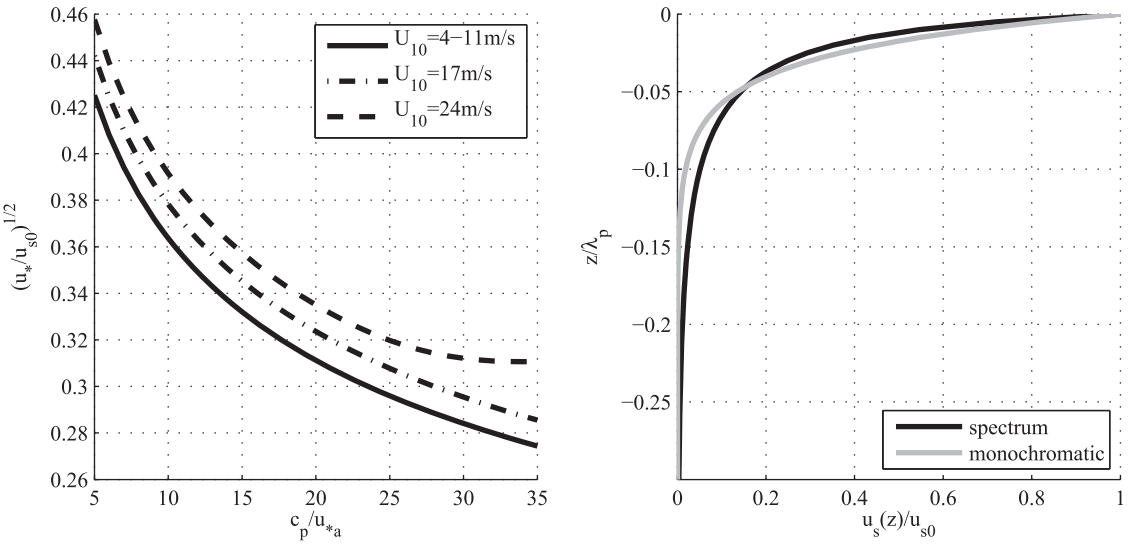

Figure 2. (left)Turbulent Langmuir number $La_t=\sqrt{u_*/u_{s0}}$ versus wave age c_p/u_{*a} and (right) normalized Stokes drift profile obtained from the integration over the wave spectrum (black) and an estimate for a monochromatic wave with an equivalent wavelength $\lambda_e=0.1\pi\lambda_p$ (gray).

The model for the unidirectional wave height spectrum $\phi(\omega)$ is based on a parametric spectrum for wind-driven equilibrium seas [*Donelan et al*., 1985] with parameters adopted from *Komen et al*. [1996]. The two input parameters are the wind speed at 10 m height U_{10} and peak radian frequency ω_p, where ω is the radian frequency,

$$\phi(\omega)=\alpha g^2\omega^{-5}\frac{\omega}{\omega_p}\exp\left(-\left[\frac{\omega}{\omega_p}\right]^{-4}\right). \tag{17}$$

The gravitational acceleration is $g = 9.81$ m/s^2 and the parameter α is $\alpha=0.006(\omega_p U_{10}/g)^{0.55}$. Equivalently, the two input parameters can be expressed in terms of the air friction velocity u_{*a} and wave age c_p/u_{*a}, where c_p is the peak wave frequency and $u_{*a}=\sqrt{\tau/\rho_a}$ (the surface wind stress is τ and the density of air is ρ_a). In this study, τ and U_{10} are uniquely related through the drag coefficient parameterization from *Large and Pond* [1981]. We implement here only the one-dimensional (1-D) spectrum because our results differ only slightly from those obtained for the full 2-D spectrum. The spectrum is used only for the energy containing frequency range with maximum frequency $\omega_{\max}=4\omega_p$. The short-wave tail may be important for small-scale near-surface LT; however, it is not well constrained [e.g., *Kukulka and Hara*, 2005, 2008a, 2008b] and will therefore be investigated in a separate study.

The Stokes drift profile $u_s(z)$ is computed from the wave spectrum following *Huang* [1971] and imposed in the LES model. For lower winds, the turbulent Langmuir number La_t depends only on wave age (Figure 2, left). For greater U_{10}, there is a small wind speed dependency because the drag coefficient depends on U_{10}, shifting the peak frequency through the wave age relationship. The Stokes drift profile normalized by its surface value and z scaled by the peak wavelength $\lambda_p=2\pi g\omega_p^{-2}$ is not dependent on wind speed or wave age (black line in Figure 2, right). An estimate for a monochromatic wave with an equivalent wavelength $\lambda_e=0.1\pi\lambda_p$ (gray line in Figure 2, right) is close to the estimate obtained by integrating over the full wave spectrum.

3.3. Breaking Waves

Our approach is an extension of the work by *Craig and Banner* [1994], who specified a TKE surface flux F due to BW in a horizontally averaged model. It simplifies the stochastic BW model from *Sullivan et al*. [2007]. We impose a horizontally uniform BW work term, $W(z)$, that inputs TKE into the SGS motion (see discussion by *McWilliams et al*. [2012]),

$$\frac{\partial e}{\partial t}+\bar{u}_j\frac{\partial e}{\partial x_j}=\ldots-\epsilon+W(z). \tag{18}$$

The vertically integrated W is equal to the total TKE flux from BWs, i.e.,

$$\int_{-\infty}^{0} W(z)dz=F. \tag{19}$$

Because the shape of $W(z)$ is not well constrained and the largest contribution is near the surface, we specify $W(z)=c_F\delta(z)$, where δ is the Dirac delta function and c_F denotes a constant coefficient constrained by (19), so that BW TKE input is imposed as a surface flux.

In equilibrium wind-wave conditions considered in this study, the energy loss by BWs F is approximately balanced by the total wind energy input and can be expressed as [*Komen et al.*, 1996]

$$F=g\int_0^{\omega_{\max}}\beta\phi(\omega)d\omega. \tag{20}$$

The wave growth rate β is adopted from *Plant* [1982]

$$\beta=c_\beta u_*^2 c^{-2}\omega, \tag{21}$$

for $c/u_{*a}<35$, and $\beta=0$ otherwise. The wave phase speed c is $c=g/\omega$, $u_*=\sqrt{\tau/\rho_w}$ denotes the waterside friction velocity, ρ_w is the density of water, and $c_\beta=(32\pm16)$ denotes a nondimensional growth rate coefficient with large uncertainties. The "effective" phase speed Fu_*^{-2} [*Terray et al.*, 1996] computed for our parameters and normalized by peak phase speed is consistent with previous approaches for a typical range of u_{*a}/c_p (inverse wave ages) in equilibrium ocean wind sea conditions (Figure 3 (left), compare to Figure 6 in *Terray et al.* [1996]). Note that $Fu_*^{-2}c_p^{-1}$ is roughly proportional to inverse wave age u_{*a}/c_p and consequently Fu_*^{-2} is roughly proportional to u_*. Indeed, Fu_*^{-3} does only change by a factor of about two for the wave age range from 5 to 35 for a given wind speed (Figure 3, right). Since a relevant velocity scale for turbulent mixing is related to $F^{1/3}$ based on dimensional analysis, variations by a factor of two in F only causes a roughly 25% change in turbulent velocity scale due to BWs. Since in our approach only F characterizes BW effects, an approximate BW turbulence velocity scale is related to u_* with relatively weak wave age dependence, similar to shear-driven boundary layer turbulence, which is consistent with the analysis from *Craig and Banner* [1994].

A characteristic length scale λ_b of BWs that dominantly contribute to F can be defined such that waves with $\lambda\le\lambda_b$ contribute 50% to F. From (20) with (17), it follows that $\lambda_b\approx 0.1\lambda_p$. This result differs from the *Sullivan et al.* [2007] BW model, which assumes that λ_b increases and the number of breakers decreases with decreasing wave age. Details of the dependence of λ_b and F on wind and wave conditions are uncertain because our knowledge of wind and wave coupling dynamics is incomplete. For example, for very young seas, it has been shown that λ_b approaches λ_p based on wind and wave coupling theory [*Kukulka et al.*, 2007; *Kukulka and Hara*, 2008b].

3.4. Parameter Space and Details of Model Setup

The foregoing discussion suggests that the turbulent diffusivity (8) and (10) with (11), taking BW and LT effects into account, can be expressed in nondimensional form as

$$\frac{A(z)}{hu_*}=\text{function}\left(\frac{z}{h},\frac{c_p}{u_{*a}},\frac{\lambda_p}{h},\frac{z_0}{h}\right). \tag{22}$$

For the concentration profiles, it follows from (3) that

$$\left(\frac{C(z)}{C(0)}\right)^{\frac{u_*}{w_b}}=\text{function}\left(\frac{z}{h},\frac{c_p}{u_{*a}},\frac{\lambda_p}{h},\frac{z_0}{h}\right). \tag{23}$$

Therefore, in theory, it suffices to examine a single value for w_b because solutions are self-similar. Practically, buoyant tracer concentrations and their vertical gradients should be large enough; through trial and error, we set by default $u_*/w_b=1.22$.

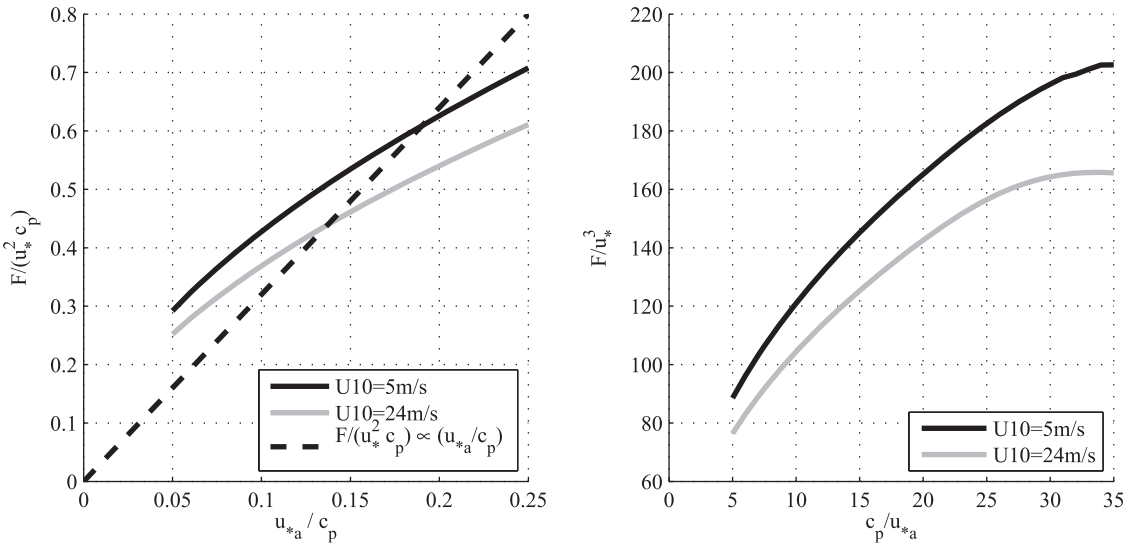

Figure 3. Normalized TKE input F: (left) $F/(u_*^2 c_p)$ versus inverse wave age u_{*a}/c_p and (right) F/u_*^3 versus wave age c_p/u_{*a}.

Sensitivity of results due to the parameters z_0 and h are not investigated in this study. The roughness length z_0 is an internal LES parameter determined from the SGS closure model. The boundary layer depth h is approximately constant and coincides with the depth where local density gradients peak. Parameters are chosen (see section 3.1), so that the buoyancy entrainment due to shear at the mixed layer base is relatively weak, because the e-folding length of the Ekman current, about 0.25 u_*/f, does not exceed h [*McWilliams et al.*, 1997]. Note, however, that more generally the boundary layer depth depends on u_*/f, in which case the nondimensional parameter fh/u_* would need to be included in (22) [*McWilliams et al.*, 2012].

This leaves us with the wave age and wind stress as the main parameters to be investigated in this study. Note that changes in wind stress cause variation in λ_p for given wave age, so that a nondimensional parameter that captures wind stress variations can be expressed in terms of λ_p/h. The range of wind stress values is chosen so that the Stokes drift is confined to the mixed layer and no significant buoyancy entrainment occurs over time integration of one inertial period (see above). These constraints result in a limited wind speed range of $U_{10}=5-10$ m/s, for which the drag coefficient is constant and the relation between wave age and La_t unique. The wave age is examined for fully developed seas with $c_p/u_{*a} \approx 35$ to younger seas, so that the Stokes drift profile is resolved by the numerical grid. Only for comparison with previous studies, we also simulate different wind and wave conditions. All LES runs for this study are summarized in Table 1.

4. Results

4.1. Model Assessment

4.1.1. Without Wave Effects

Without wave effects, the LES solutions agree well with the analytic solutions (4) and (7) for different w_b and u_* (Figure 4) with $z_0 = 0.5$ m and $c_0 = c_w = 1$ (solid wall boundary layer turbulence). By default, we set $z_0 = 0.5$ m for the analytic Reynolds-averaged model. The empirically determined value for z_0 is consistent with previous estimates in the range of 0.1–8.0 m [*Craig and Banner*, 1994] and also consistent with the subgrid-scale parameterization (16) for which $z_0 \approx K_\theta/(\kappa u_*)=0.6$ m, where we have used the near-surface subgrid-scale TKE $\langle e \rangle/u_*^2 \approx 1.1$ based on LES results. The resolved turbulent kinetic energy exceeds 75% of the total (resolved + subgrid scale) TKE even at the first grid points where subgrid-scale fluxes are most important. The total TKE varies between $2 < TKE/u_*^2 < 5$, which is consistent with previous estimates for shear-driven boundary layer turbulence, e.g., $TKE/u_*^2 = 1/0.55^2 = 3.3$ [e.g., *Pope*, 2008]. The LES solutions for C suggest that the vertical resolution is sufficient for our default $u_*/w_b = 1.22$ as $\Delta z/d$ (a numerical Peclet number) varies significantly; yet, LES C profiles are consistent with (4) and (7) (Figure 4).

It is important to keep in mind that our and previous upper ocean LES approaches to incorporating breaking waves impose z_0 through the subgrid-scale model and that more complete approaches need

Table 1. Summary of All LES Runs[a]

U_{10} (m s^{-1})	u_* (cm s^{-1})	conditions	c_p/u_{*a}	Figure
5	0.61	ST	n/a	4
5	0.61	LT/BW	10	10
5	0.61	LT/BW	20	10
5	0.61	LT/BW	25	10
5	0.61	LT/BW	30	10
5	0.61	LT/BW	35	10
7	0.89	LT/BW	5	5
7	0.89	BW	10	12
7	0.89	LT	10	12
7	0.89	LT/BW	10	5, 10, 12
7	0.89	LT/5XBW	10	12
7	0.89	LT	20	12
7	0.89	LT/BW	20	10, 12
7	0.89	LT/BW	25	10
7	0.89	LT/BW	30	10
7	0.89	LT	35	12
7	0.89	LT/BW	35	5, 10, 12
10	1.22	ST	n/a	4
10	1.22	BW	35 [0]	10
10	1.22	LT/BW	5	10
10	1.22	LT/BW	8	10
10	1.22	LT/BW	10	10
10	1.22	LT/BW	12	10
10	1.22	LT/BW	15	10
10	1.22	LT/BW	20	10
10	1.22	LT/BW	27	10
10	1.22	LT/BW	30	10
10	1.22	ST	n/a	9
10	1.22	BW	35 [0]	9
10	1.22	LT	35	9
10	1.22	LT/BW	35	9, 10
15	1.87	LT/BW	5	5
15	1.87	LT/BW	10	5
15	1.87	LT/BW	35	5
15	1.87	ST	n/a	6, 7, 8
15	1.87	BW	30	6, 7, 8
15	1.87	LT	30	6, 7, 8
15	1.87	LT/BW	30	6, 7, 8

[a]For BW only runs, the wave age is also assigned to zero [0], see main text. The 5XBW indicates that the default breaking wave input is enhanced by a factor of five.

to be taken to model z_0. Given the wide range of z_0, we perform below a sensitivity analysis based on analytic solutions. This analysis also suggests z_0 is likely not a critical parameter in the presence of relatively large-scale LT, which are well resolved by the LES model and do not strongly depend on subgrid-scale parameterizations.

4.1.2. Near-Surface Dissipation Rates

Previous observational [*Terray et al.*, 1996] and modeling [*Craig and Banner*, 1994] studies have shown that oceanic near-surface TKE dissipation rates are significantly larger than those expected for a solid wall surface boundary layer. To model previous measurements, we run our LES model with the effects of Stokes drift and BWs at six different conditions to cover a realistic range of wind and wave conditions consistent with the observations (Table 1). LES model results generally agree with previous measurements, although there is significant scatter in observations and simulations (Figure 5). Our results suggest that the scatter in the observations is partially due to different wind and wave conditions. LES model results agree the least with the best fit solution for the field conditions not observed during the experiment in Lake Ontario (circles, $U_{10} = 15$ m/s, $c_p/u_{*a} = 35$) [*Terray et al.*, 1996]. Clearly, more observations are needed for a more comprehensive comparison.

4.1.3. Comparison With a More Complete Approach

To compare our model results with the more complete approach from *Sullivan et al.* [2007], we perform simulations for their prescribed default condition with $U_{10} = 15$ m/s and wave age $c_p/u_{*a} = 30$, resulting in $La_t = 0.3$ and LT favorable conditions. Our simulation setup uses a smaller domain size with less grid points and a different parameterization of the empirical wave spectrum, so that both u_s and F differ in details. Following *Sullivan et al.* [2007], we perform four different simulations, including without wave effects, with only LT effects, with only BW effects, and with both wave effects (Table 1).

Consistent with results from *Sullivan et al.* [2007], we find that BWs enhance near-surface dissipation rates by 2 orders of magnitude (Figure 6, only BW: thin solid lines, BW and LT: lines with circles). Stokes drift causes larger dissipation at greater depth. Without wave effects (dash-dotted lines), both models predict near-surface dissipation that is consistent with typical wall layer scaling (thick black line). Both wave effects also increase the near-surface TKE (Figure 7, only BW: solid lines, BW and LT: lines with circles). Simulations with BW effects have a significantly higher surface TKE and SGS percentage of the total TKE than the cases without wave effects or just Stokes drift (without waves: dash-dotted, only LT: lines with triangles). Although our SGS TKE values are larger at the surface because we flux TKE from breaking waves at the first grid point, the SGS contribution accounts for a similar percentage of the total TKE and TKE rapidly decreases to similar values from *Sullivan et al.* [2007]. It is interesting to examine next the velocity variance contributions to TKE, which characterize wave-driven upper ocean turbulence (Figure 8). Resolved velocity variance profiles overall agree well with those obtained from *Sullivan et al.* [2007], suggesting that we capture to first-order TKE dynamics expected for a stochastic BW field. The

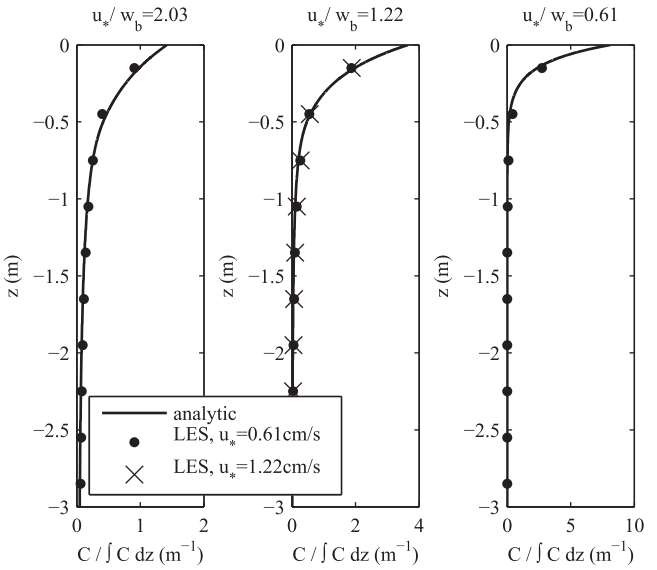

Figure 4. Analytic (lines) and LES (symbols) solutions without wave effects for u_*/w_b = (left) 2.03, (middle) 1.22, and (right) 0.61. By default, u_* is set to u_* = 0.61 cm/s (U_{10} = 5m/s) for the LES solutions (dots). To examine the self-similar behavior of solutions, we also considered an LES solution with u_*/w_b = 1.22 and u_* = 1.22 cm/s (U_{10} = 10 m/s) (crosses in middle plot). For the analytic solutions, A is constant at $A=\kappa z_0 u_*$ with z_0 = 0.5 m.

elevated vertical and cross-wind velocity variances are a typical signature of LT (right and middle plots, respectively, in Figure 8). Note, however, that simulated vertical velocity variances are significantly larger than those observed [*D'Asaro*, 2001; *D'Asaro et al*., 2014], indicating that the model forcing may be much stronger than that for the observed ocean conditions. In spite of its large surface contribution to total TKE, the BW effect is relatively small because turbulent motion due to breaking is not represented in model forcing at resolved scales. Differences in the results of the two approaches are partially explained by differences in the implementation (grid resolutions, Stokes drift profiles, TKE input). Overall, the detailed comparison for this particular case suggests that our simplified approach captures some important features of the more complete approach from *Sullivan et al*. [2007]. This finding is consistent with scaling arguments that suggest that the energy contribution due to the resolved stochastic events is relatively small in the *Sullivan et al*. [2007] approach, so that most BW energy transfer occurs on unresolved subgrid scales (Appendix A). Nevertheless, the *Sullivan et al*. [2007] approach

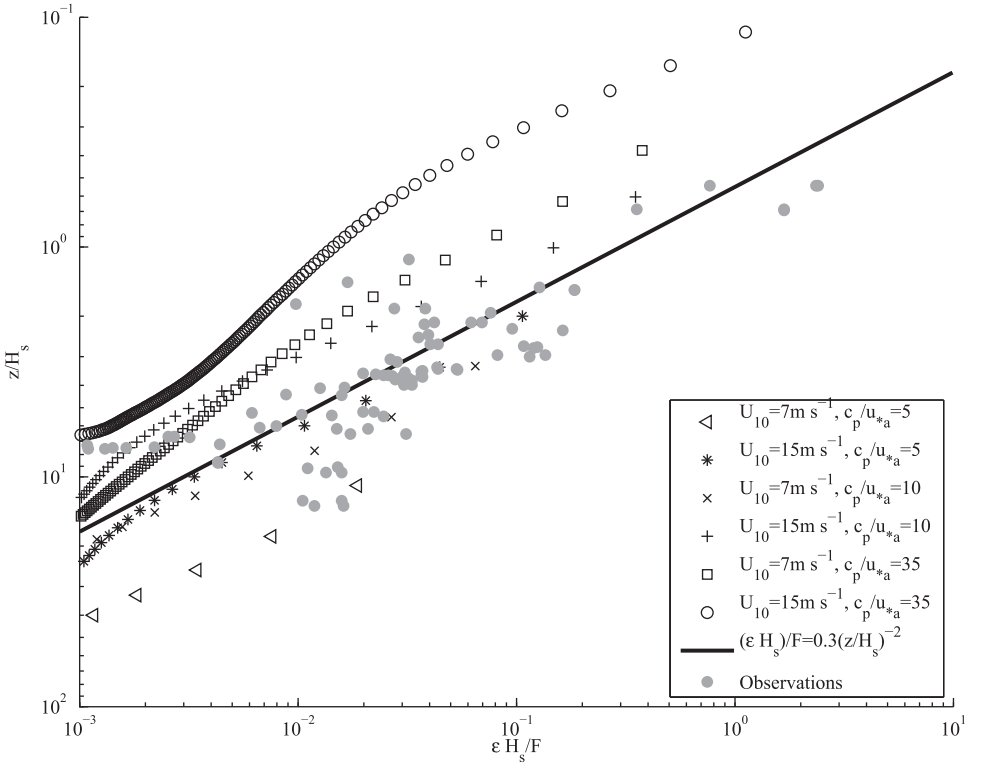

Figure 5. Comparison of model results (black symbols) and observations from *Terray et al.* [1996] (gray dots) for normalized TKE dissipation rate ε depth profiles at different wind and wave conditions. Our symbols represent LES results for different U_{10} and wave age c_p/u_{*a}. The solid line is a best fit to observations provided by *Terray et al.* [1996].

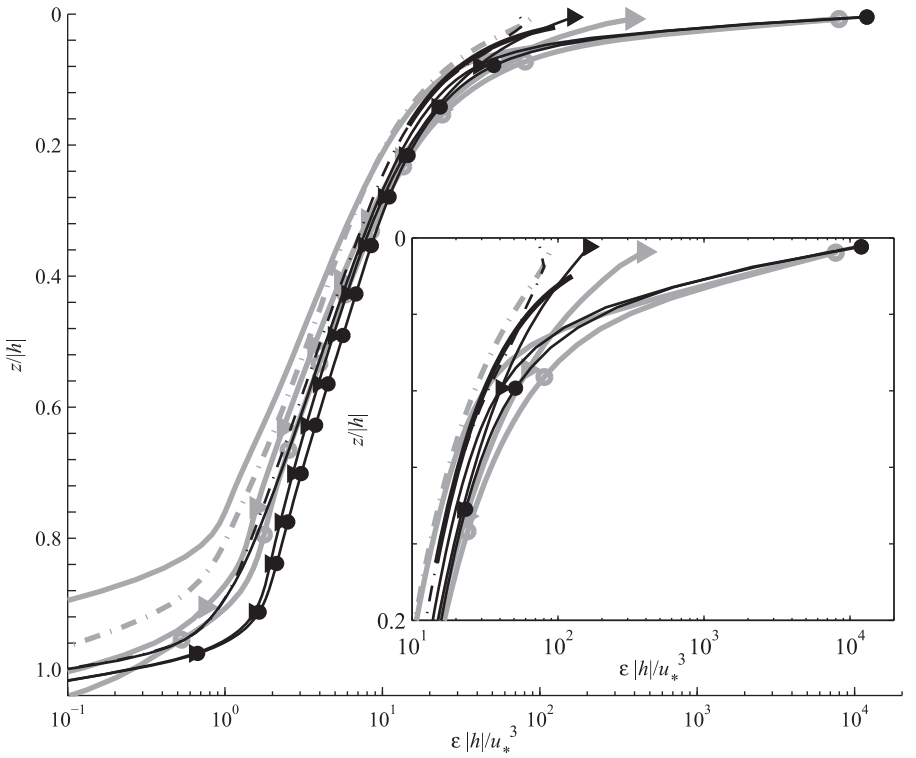

Figure 6. Comparison of normalized TKE dissipation rates ε. Our results (black), results from *Sullivan et al.* [2007] (gray) without wave effects (dash-dot line), Langmuir turbulence only (triangles), breaking waves only (solid line without symbols), and both wave effects (circles). The thick solid black line is the estimate for wall layer scaling, $\varepsilon = u_*^3/(\kappa|z|)$.

captures locally enhanced SGS energy injection events and a long-lived coherent breaking wave vortex [*Sullivan et al.*, 2004], whose impacts on buoyant tracer distributions have yet to be systematically assessed.

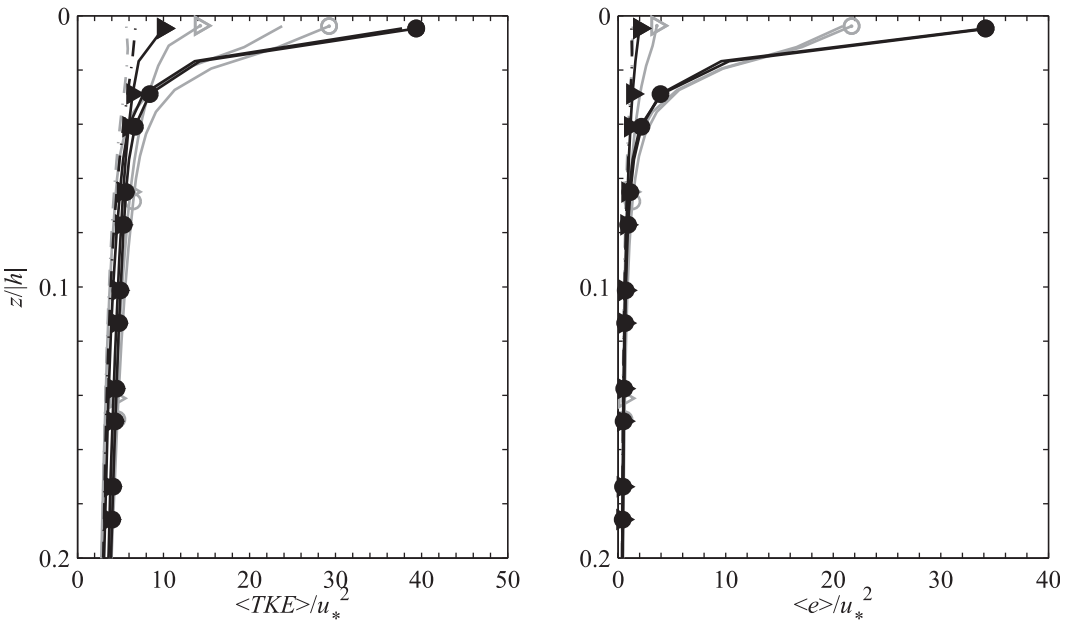

Figure 7. Comparison of (left) near-surface total and (right) subgrid-scale turbulent kinetic energy. Our results (black), results from *Sullivan et al.* [2007] (gray) without wave effects (dash-dot line), Langmuir turbulence only (triangles), breaking waves only (solid line without symbols), and both wave effects (circles). Note that the breaking wave only solution may coincide with the solutions for both wave effects.

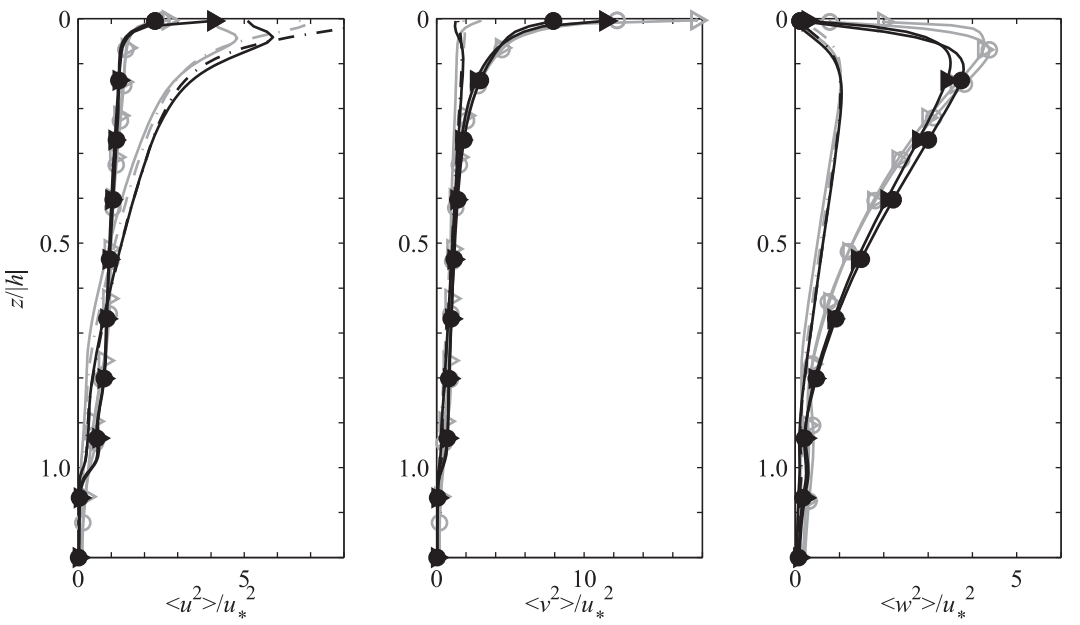

Figure 8. Comparison of resolved velocity variance. Our results (black), results from *Sullivan et al.* [2007] (gray) without wave effects (dash-dot line), Langmuir turbulence only (triangles), breaking waves only (solid line without symbols), and both wave effects (circles).

4.2. BW and LT Effects on Vertical Tracer Distributions

To understand the individual and combined effects of BW and LT on vertical tracer distributions, we examine in detail the case for $U_{10} = 10$ m/s and $c_p/u_{*a}=35$ (Figure 9). Without wave effects, the LES solution (black dots) agree well with the analytic solution (gray line) for $c_0 = c_w = 1$, so that we recover the KPP model with near-surface mixing for a solid wall boundary layer. For enhanced wave mixing, on the other hand, we expect $c_0 > 1$ or $c_w > 1$. Indeed, for BW only, we find a good fit between the analytic and LES solutions for $c_0 = 4$ and $c_w = 1$ (BW plot in Figure 9). This suggests that BW mainly enhances near-surface mixing, but does not strongly influence transport at greater depth, which is consistent with the idea that enhanced BW mixing is confined to the surface [*Terray et al.*, 1996].

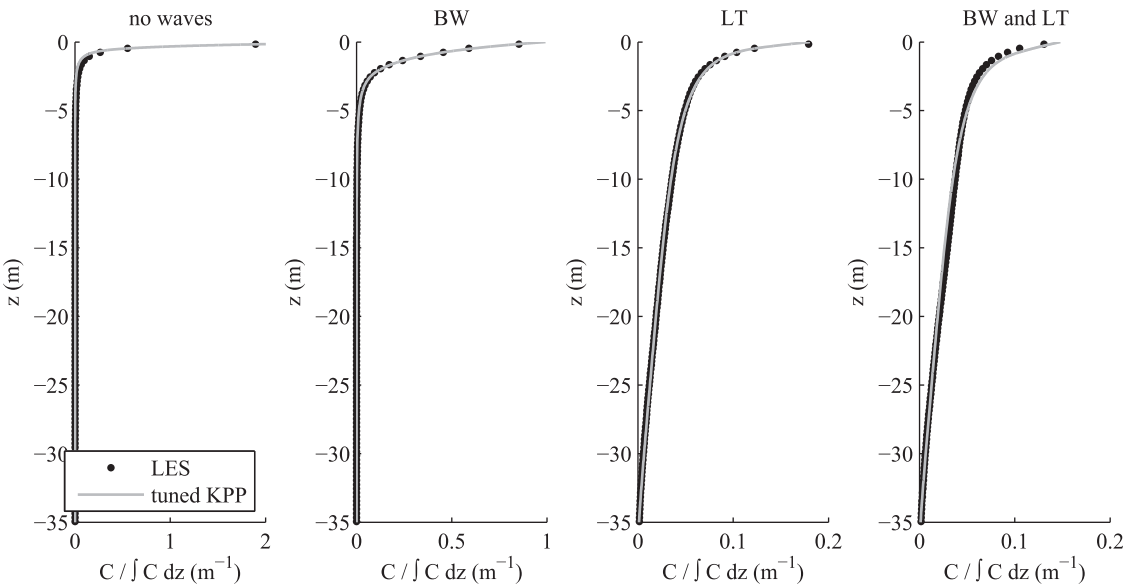

Figure 9. LES solutions (dots) for $U_{10} = 10$ m/s and $c_p/u_{*a}=35$ with and without wave effects and analytic solutions (gray lines) for the modified KPP model with the parameters c_0 from (10) and c_w from (11): $(c_0,c_w) = (1,1)$ (no waves), $(c_0,c_w) = (4,1)$ (BW), $(c_0,c_w) = (5,6)$ (LT), and $(c_0,c_w) = (9,6)$ (BW and LT).

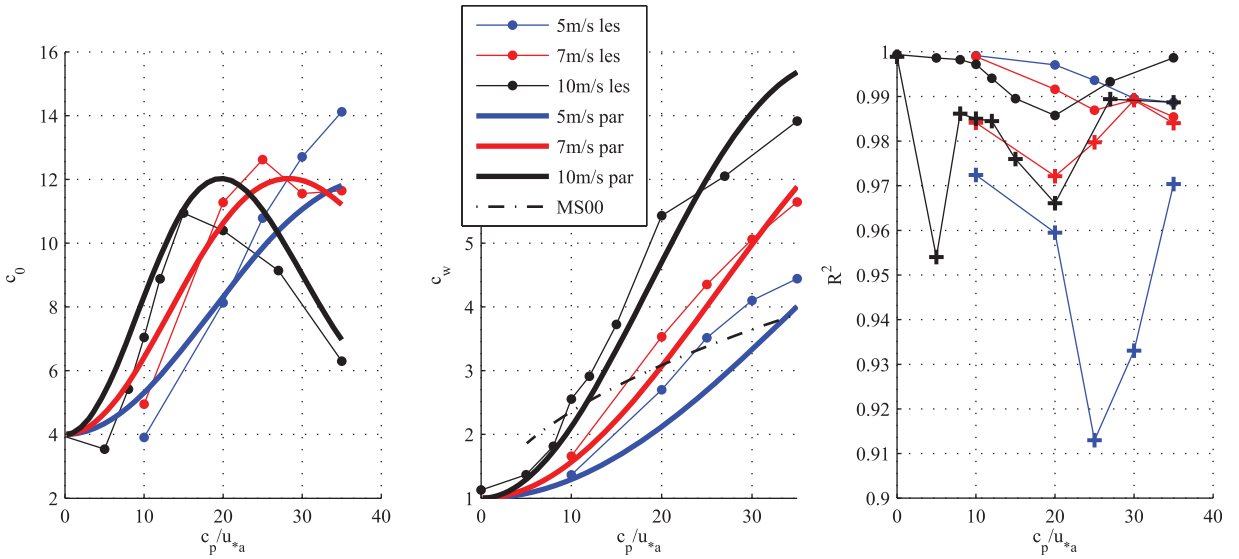

Figure 10. Coefficients (left) c_0 and (middle) c_w determined from each individual LES experiment by minimizing the squared difference between LES solutions (with BW and LT) and analytic concentration profiles (dots). Parameterized c_0 based on (27) and c_w based on (28) (solid thick lines left and middle plots, respectively). Our c_w is consistent with the one from *McWilliams and Sullivan* [2000] (MS00, dash-dotted line). (right) R^2 for case specific coefficients (dots) and for the parameter model (pluses).

If only LT effects are taken into account, we find reasonable agreement between LES and analytic solutions for $c_0 = 5$ and $c_w = 6$ (LT plot in Figure 9). This suggests that LT influences both transport near the surface and at greater depth. Enhanced deep mixing causes the buoyant tracer to be submerged deeply and to be distributed throughout the whole water column. LES solutions with combined LT and BW effects do not significantly influence deep mixing relative to LT only solutions but appear to enhance near-surface mixing relative to solutions with either BW only or LT only (Figure 9, right). Consequently, c_w is close to the LT only value with $c_w = 6$ and c_0 increases further to $c_0 = 9$. Note that the effects of LT and BW are not simply additive, because in our approach BW TKE injection dissipates small-scale LT structures [*McWilliams et al*., 2012]. Thus, one may expect that enhanced mixing due to BW compensates for impeding small-scale near-surface LT. This example provides some intuitive insights, facilitating a more systematic investigation of c_0 and c_w for different conditions.

4.3. Dependence on Wind and Wave Conditions

We will next examine how the turbulent eddy diffusivity $A(z)$, i.e., the coefficients c_0 and c_w, depends on wind (U_{10}) and wave (c_p/u_{*a}) conditions. We determine objectively c_0 and c_w by minimizing the squared difference between $C(z)$ obtained from the LES and analytic models. The near-surface coefficient c_0 and deep mixing coefficient c_w are determined as functions of wave age for three wind speeds U_{10}=5, 7, and 10 m/s (dots in left and middle plots of Figure 10). The analytic solutions with the best fit coefficients c_0 and c_w capture over 98% of the C variance of the LES solutions (dots in the right plot of Figure 10), which suggests that the simple analytic model accurately captures first-order turbulent transport characteristics.

As the wave age increases, both coefficients initially increase from roughly the BW only value (which is assigned wave age zero) for all wind speeds, indicating that LT enhances both near-surface and deep transport. The enhanced increase for greater U_{10} is perhaps at first surprising because La_t does not depend on U_{10} for our conditions (Figure 2). However, the Stokes drift depth decay scale, related to λ_p, increases with U_{10} for constant La_t, influencing Langmuir turbulence dynamics [*Polton and Belcher*, 2007; *Harcourt and D'Asaro*, 2008]. One interpretation of the decrease in c_0 for the two larger wind speeds and wave ages exceeding a value of about 20 (red and black dots in left plot of Figure 10) is that Langmuir cells grow larger, so that enhanced near-surface mixing transitions into deep mixing.

Note also that for elevated deep mixing, i.e., larger c_w, the coefficient c_0 is less important because the transition depth z_T from constant A_0 to depth varying $A(z)$ is shallower. Recall that the details of A_0 are less

important for buoyant tracers with $w_b < w_*$ because deep mixing critically influences vertical tracer distributions. Let us examine the maximum deep A

$$\frac{A_{\max}}{u_* h} = \frac{4}{27}\frac{w_*}{u_*} = \frac{4\kappa}{27} c_w \approx 0.0667 c_w. \tag{24}$$

This value is consistent with the eddy viscosity K_m (for momentum) from *Sullivan et al*. [2007], which was determined for fully developed sea conditions with $U_{10} = 15$ m/s. In their study, $(K_m)_{\max}/(u_* h)$ increases from a value of about 0.05 without LT effects by a factor of roughly four with LT effects. Our c_w is also consistent with the proposed one from *McWilliams and Sullivan* [2000], who suggested $c_w = (1 + 0.08 La_t^{-4})^{1/2}$ based on limited LES results (dash-dotted line in Figure 10, middle). For this comparison, we exploit the unique relation between wave age and La_t for $U_{10} \leq 10$ m/s (Figure 2). For constant wind, our c_w increases more strongly with wave age or inverse La_t because in this study λ_p/h increases concurrently, enhancing LT [*Harcourt and D'Asaro*, 2008].

Such large enhancement factors c_0 and c_w, which increase by up to 1 order of magnitude depending on wind and wave properties, are remarkable and have critical implications for the vertical distribution of buoyant tracers: wave-driven mixing is equivalent to a shear-driven boundary layer with rise velocity reduced by 1 order of magnitude.

4.4. Wave-Dependent Parameterization

A physically motivated parameterization for A can be developed by assuming that near-surface turbulence, characterized by A_0, is influenced by shear, BW and LT, and that deep turbulent transport, characterized by w_*, is mainly influenced by shear or LT. We may then express

$$A_0 = c_0^{st} \kappa z_0 u_* + z_{\mathrm{bw}} F^{1/3} + c_0^{\mathrm{lt}} \lambda_p u_*. \tag{25}$$

The first right-hand-side term is A_0 for a shear-driven boundary layer modified in the presence of waves by the factor c_0^{st} (without wave forcing $c_0^{st} = 1$). The second term follows from dimensional analysis where $F^{1/3}$ is a BW velocity scale and z_{bw} is a BW length scale, which is not explicitly modeled so that $z_{\mathrm{bw}} \propto z_0$ in our approach. Because $F^{1/3}/u_* \approx$constant (see discussion above), the first and second terms can be combined to $\gamma_0^{\mathrm{bw}} z_0 u_*$, where γ_0^{bw} is an approximately constant enhancement factor due to BW. The last term of equation (25) parameterizes LT and takes into account a length scale due to waves λ_p, motivated by our LES results. Note that the velocity scale u_* and the length scale λ_p are based on the imposed external forcing parameters and should not be simply interpreted as scales characterizing LT, so that we expect the coefficient c_0^{lt} to depend on wave properties [*Plueddemann et al*., 1996; *Smith*, 1998; *Li et al*., 2005; *Polton and Belcher*, 2007; *Harcourt and D'Asaro*, 2008; *Grant and Belcher*, 2009]. Dynamically, λ_p is related to the Stokes drift shear decay scale (see section 3.2 and Figure 2), which is critical in TKE Stokes drift shear production. For smaller λ_p/h, this TKE production is confined more closely to the surface, while for sufficiently large λ_p/h, the TKE production vanishes if the Stokes drift shear across the mixed layer approaches zero. Taking λ_p as a Stokes drift decay scale, *Harcourt and D'Asaro* [2008] showed that LT effects first increase with λ_p/h consistent with our results. The anticipated increase in transport is captured by (25) if c_0^{lt} is approximately constant for small λ_p/h. Furthermore, LT decreases once λ_p/h is sufficiently large because of the weak Stokes drift shear across the mixed layer [*Polton and Belcher*, 2007]. We model this decrease for large λ_p/h as

$$c_0^{\mathrm{lt}} = \gamma_{01} \exp\left(-\gamma_{02}[\lambda_p/h]\right), \tag{26}$$

where γ_{01} and γ_{02} are empirical constants, so that A_0 is finally expressed as

$$\frac{A_0}{u_* h} = \gamma_0^{\mathrm{bw}} \frac{z_0}{h} + \gamma_{01} \exp\left(-\gamma_{02}\left[\frac{\lambda_p}{h}\right]\right)\frac{\lambda_p}{h}. \tag{27}$$

This simple physically motivated parameterization is consistent with LES results with only three empirical constant coefficients $\gamma_0^{\mathrm{bw}} = 1.60, \gamma_{01} = 0.145, \gamma_{02} = 1.33$ (thick solid lines in left plot of Figure 10). Note that this parameterization depends implicitly on La_t because $\lambda_p/h = u_*^2/(gh)$function (La_t).

Applying similar ideas for parameterizing deep mixing, but assuming that BW effects are small, we express w_* as

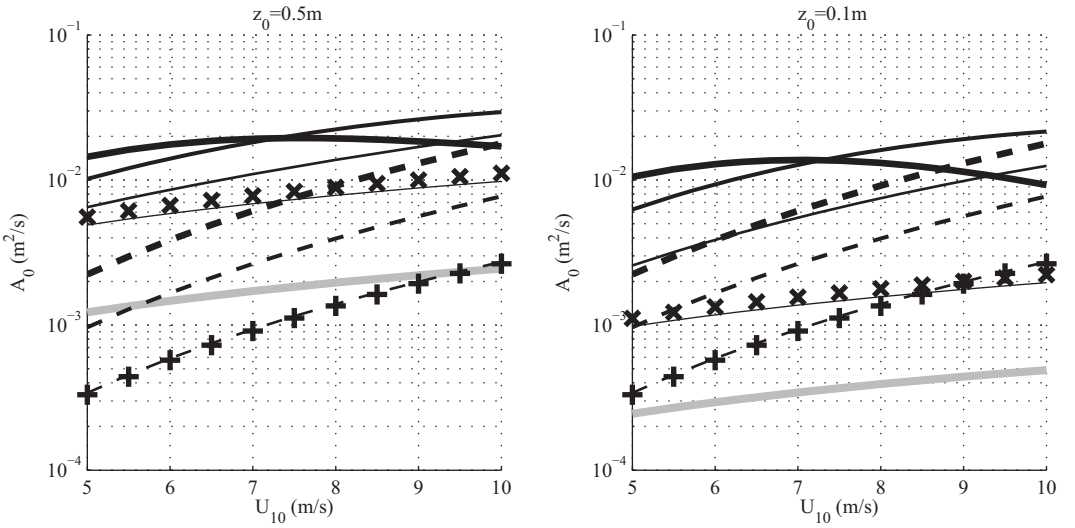

Figure 11. Comparison of various A_0 estimates: this study (black solid lines) with (left) $z_0 = 0.5$ m and (right) $z_0 = 0.1$ m for wave ages 0 (no LT), 10, 20, and 35 (wave age increases with line width), solid wall boundary layer (gray line), analytic solution from *Craig and Banner* [1994] (crosses) empirical estimate from *Li and Garrett* [1995] (pluses), and empirical estimate from *Thorpe et al.* [2003] (black dashed lines) for wave ages 10, 20, and 35 (wave age increases with line width).

$$\frac{w_*}{u_*} = \kappa + \gamma_{w1} \exp\left(-\gamma_{w2}\left[\frac{\lambda_p}{h}\right]\right)\frac{\lambda_p}{h}. \tag{28}$$

This parameterization also agrees reasonably well with LES results (thick solid lines in middle plot of Figure 10). To parameterize w_* only two additional empirical coefficients $\gamma_{w1} = 2.49$ and $\gamma_{w2} = 0.333$ are used, so that solutions converge to shear-driven solutions for $\lambda_p/h \rightarrow 0$. Furthermore, this parameterization is consistent with the no-wave and short-wave limits from *Harcourt and D'Asaro* [2008], which converge to shear-driven turbulence.

Analytic tracer profiles for the parameterized A_0 and w_* capture for most cases over 95%, but never less than 91%, of the LES $C(z)$ variance (pluses in right plot of Figure 10). The analytic solution with A parameterized based on (27) and (28) will be applied for the remaining discussions.

4.5. Near-Surface Mixing A_0

It is interesting to compare our parameterized A_0 (solid black lines in Figure 11 for wave ages "0" [defined as no LT], 10, 20, and 35) to previous estimates. Recall that wave effects enhance A_0 by the factor c_0 relative to shear-driven boundary layer turbulence (gray lines in Figure 11). For weak LT effects (young seas), A_0 critically depends on z_0 because A_0 is roughly proportional to z_0 according to (27) (compare left and right plots in Figure 11). As LT effects increase, solutions depend only weakly on z_0 because LT structures are resolved and near-surface boundary layer parameterizations are less significant.

Our A_0 is consistent with the surface momentum eddy viscosity $(K_m)_0$ from *Sullivan et al.* [2007], who found that $(K_m)_0/(u_*h)$ systematically increases from (a) no wave effects, (b) BW only, (c) LT only, to (d) both BW and LT effects from a value of about $(K_m)_0/(u_*h) \approx 0.005$ to roughly 0.020 for fully developed sea conditions and $U_{10} = 15$ m/s. In this study, we find $A_0/(u_*h) \approx 0.005$ without wave effects and $A_0/(u_*h) \approx 0.030$ for combined LT and BW effects for $U_{10} = 10$ m/s and fully developed seas. Because $A_0/(u_*h) = c_0\kappa z_0/h \approx 0.005c_0$, this indicates that the roughness length z_0 and the enhancement factor c_0 are consistent with results from *Sullivan et al.* [2007]. However, it is important to keep in mind that the momentum eddy viscosity differs from our A_0 because momentum source terms have vertical structure in the approach from *Sullivan et al.* [2007].

By balancing TKE dissipation with vertical TKE transport, the following analytic expression for the surface eddy diffusivity is obtained from the *Craig and Banner* [1994] model

$$A_0 = (\kappa z_0)\left[F^{1/3}(3B/S_q)^{1/6}\right] S_m, \tag{29}$$

where the empirical constant coefficients S_m, S_q, B are given by $S_m=0.39, S_q=0.2, B=16.6$. The term in the first brackets is a surface mixing length and the term in the square brackets is the square root of twice the surface TKE. The BW TKE flux F is set to $F=100u_*^3$ by *Craig and Banner* [1994]. This estimate (crosses in Figure 11) agrees well with our estimate with only BW effects (wave age 0), suggesting that TKE transport is balanced by dissipation for the LES solutions and that BW effects are only weakly dependent on wave age consistent with the discussion above.

Thorpe et al. [2003] suggested the following empirical wave age-dependent model for A_0 (dashed lines in Figure 11)

$$A_0=1.5\kappa H_s u_* \quad \text{for} \quad |z| < 1.5H_s. \tag{30}$$

This formula assumes that the mixing length is proportional to the significant wave height H_s, which is parameterized as $H_s=0.96g^{-1}(c_p/u_{*a})^{3/2}u_{*a}^2$. For constant wave age, A_0 is proportional to u_*^3, which is consistent with the empirical model from *Li and Garrett* [1995] (pluses in Figure 11), which has been applied in previous studies [e.g., *Gemmrich and Farmer*, 1999; *Thorpe et al.*, 2003]. Because of the cubic wind speed dependence, A_0 will exceed the A_0 from this study for sufficiently high wind conditions. The A_0 from *Thorpe et al.* [2003] is more consistent with our result for the smaller $z_0 = 0.1$ m (Figure 11, right).

In the direct numerical simulation (DNS) approach from *Sullivan et al.* [2004], no external roughness parameters need to be imposed because all nonwave motions are resolved. In this approach, however, the Reynolds number is limited and significantly smaller than that for realistic ocean conditions. *Sullivan et al.* [2004] found that for a particular BW with λ, z_0/λ varies between 0.04 and 0.06 when breaking constitutes 80% to 100% of the total stress, resulting in a hydrodynamically rough boundary layer. For the simulated laboratory waves, z_0 is lower than the one used by *Craig and Banner* [1994], which is in the range of $z_0=0.1-8.0$ m.

Previous field observations agree with such a large value of z_0, which has been shown to scale with H_s [*Terray et al.*, 1996; *Gerbi et al.*, 2009; *Soloviev and Lukas*, 2003]. However, *Gemmrich and Farmer* [2004] pointed out that most of those estimates are determined based on TKE dissipation rates and found that $z_0 \approx 0.2$ m based on observations of turbulent temperature fine structures.

4.6. Disruption of Organized LT by BW

To understand more systematically under what conditions the enhanced near-surface mixing due to BWs may disrupt organized Langmuir circulations, it is useful to consider the nondimensional laminar Langmuir number

$$La_{\text{lam}}=[(Ak/u_*)^3(u_*/u_{s0})]^{1/2}, \tag{31}$$

that arises from "laminar theory" in which small-scale mixing is parameterized based on eddy viscosity [*Leibovich*, 1983]. Linear stability theory suggests that La_{lam} should be smaller than one for LT presence, otherwise small-scale mixing inhibits the formation of Langmuir cells [*Leibovich and Paolucci*, 1981]. Generally, it is challenging to separate contributions of A due to incoherent smaller-scale and coherent larger-scale motions [see also *Kukulka et al.*, 2012a] and to estimate the wavenumber k for a spectrum of waves. Reasonable estimates for A are given by (29) with only BW effects or, without BWs, $A=A_0=u_*\kappa z_0$. The wave number can be approximated based on the equivalent wavelength λ_e that matches reasonably well the Stokes drift profile for given u_{s0} (compare gray and black lines in right plot of Figure 2).

As an example, let us consider $U_{10} = 7$ m/s for different wave conditions. Coherent bands of vertical velocities become weaker for decreasing wave ages ($c_p/u_{*a}=35,\ 20,$ and 10 (Figure 12)), which is consistent with the increasing La_t. With only LT effects (first three top plots) finer turbulent structures are apparent relative to simulations with BW and LT effects (first three bottom plots). This is qualitatively consistent with La_{lam}, which is an order of magnitude larger with BW effects. For example, for the youngest wave age 10, $La_{\text{lam}}=0.35$ without BW effects and $La_{\text{lam}}=3.8$ with BW effects, suggesting a strong obstruction of LT by breaking waves. If the BW input is enhanced by a factor of five ($La_{\text{lam}}=8.4$,Figure 12, top right), turbulent near-surface velocities resemble the case without wave effects (Figure 12, bottom right). Considering that A is proportional to u_*z_0, these results suggest with (31) that λ_p/z_0 and La_t are key nondimensional parameters in understanding the disruption of organized LT by BW.

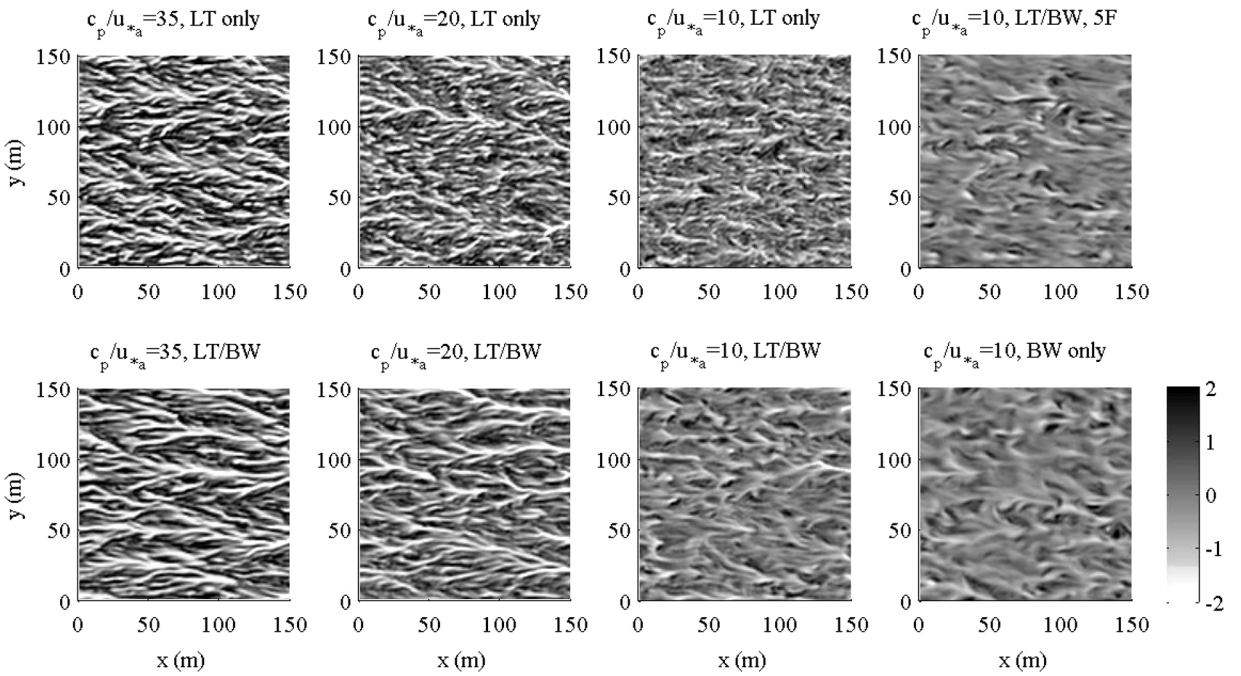

Figure 12. Near-surface vertical velocity w normalized by u_* on a horizontal plane at $z = -1.35$ m at constant $U_{10} = 7$ m/s for different wave ages c_p/u_{*a} and wave conditions. LT/BW refers to the default simulation with breaking waves and Langmuir turbulence, LT only includes only Langmuir turbulence, BW only includes only breaking waves, and 5F refers to a breaking TKE surface flux that is enhanced by a factor of five.

4.7. Surface Trapping and Deep Submergence

We specify two metrics that characterize surface trapping (or deep submergence). The first is related to the depth-weighted normalized concentration

$$T_n = 1 + \frac{2\int_{-h}^{0} zC\,dz}{h\int_{-h}^{0} C\,dz}, \tag{32}$$

which is $T_n = 0$ for a vertically homogeneous profile and $T_n = 1$ for surface trapped buoyant tracers. The second metric is the normalized buoyant tracer concentration in the upper φh surface layer (φ represents a fraction of the total depth),

$$T_\varphi = \frac{1}{1-\varphi}\left(\frac{\int_{-\varphi h}^{0} C\,dz}{\int_{-h}^{0} C\,dz} - \varphi\right), \tag{33}$$

which is $T_\varphi = 0$ for a vertically homogeneous profile and $T_\varphi = 1$ for tracers entirely trapped in the upper φh surface layer. We compute T_n and T_φ with our analytic model (3) with (8) using the parameterizations (27) and (28).

We examine the conditions for which the buoyant tracer is either nearly vertically homogeneous, i.e., $T_n \to 0$ or completely surface trapped, i.e., $T_n \to 1$ (Figure 13, left). The gray line shows solutions without wave effects and the blue line represents the BW only solutions. For fixed wind speed, the wave age increases in the following order: red (youngest sea), cyan, black, magenta, and yellow (oldest sea). Regardless of wave conditions, concentration profiles are nearly homogenous and $T_n \to 0$ for $w_b/u_* < 0.01$, even without wave effects (gray line). For $w_b/u_* > 10$, buoyancy effects overcome turbulent mixing and the tracer is surface trapped with $T_n \approx 1$. For intermediate values of w_b/u_* submergence is strongly dependent on different sea states (colored curves). For example, at $w_b/u_* = 1$, significant submergence ($T_n \approx 0.5$) occurs for $\lambda_p/h = 2.4$

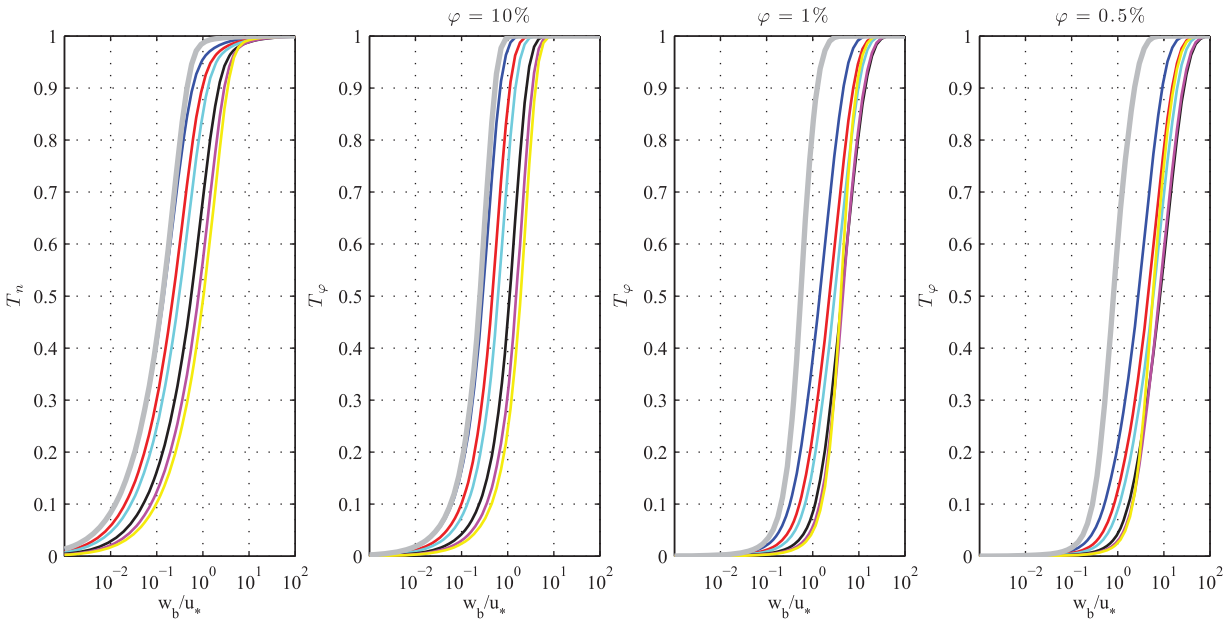

Figure 13. Measures of surface trapping T_n from (32) and T_φ from (33) based on analytic solutions of (3) with (8) using the parameterizations (27) and (28) for $z_0 = 0.5$ m and $\lambda_p/h = 0.0$ (blue, BW only), 0.1 (red), 0.2 (cyan), 0.6 (black, e.g., $U_{10} = 5$ m/s, c_p/u_{*a}=35), 1.2 (magenta, e.g., $U_{10} = 7$ m/s, c_p/u_{*a}=35), 2.4 (yellow, e.g., $U_{10} = 10$ m/s, c_p/u_{*a}=35), and solutions without wave effects (gray); $T_n = T_\varphi = 1$ for complete surface trapping and $T_n = T_\varphi = 0$ for vertical homogeneous profiles. T_n is related to a normalized depth-weighted concentration, T_φ is related to the fraction of total buoyant tracer material in the upper φh of the water column.

(yellow line, corresponding, e.g., to a fully developed sea with $U_{10} = 10$ m/s), whereas buoyant particles are nearly surface trapped without LT.

These results are consistent with the second surface trapping measure T_φ, which provides more detail on the trapping depth. For small λ_p/h (e.g., young seas), BW effects are particularly important for near-surface distributions very close to the surface with $\varphi \leq 1\%$ (third and fourth plots of Figure 13). For example, for $w_b/u_* = 1$ and $\varphi = 1\%$, T_φ drops from 0.9 without wave effects (gray curve, the tracer is nearly trapped in the upper 1% of the surface layer) to 0.4 with only BW effects so that significant tracer concentrations are at depth below 1% (blue curve). If one considers only trapping in the upper 10% of the mixed layer (second plot of Figure 13), the BW only solution (blue curve) is relatively close to the solution without wave effects (gray curve). These results suggest that observations of deeply submerged buoyant tracers, such as of microplastic marine debris, provide a signature of wave-driven upper ocean turbulence.

4.8. Near-Surface Gradients

Vertical buoyant tracer concentration gradients are critical in reactive processes and determine density stratification due to air void fractions. The largest tracer concentration gradient is at the surface and is expressed in nondimensional form as

$$\tilde{\nabla}_0 = h^2 \frac{\left(\frac{dC}{dz}\right)_0}{\int_{-h}^{0} C dz}. \tag{34}$$

To determine $\tilde{\nabla}_0$, we again apply the analytic model (3) with (8) using the parameterizations (27) and (28). Results indicate a strong dependence of $\tilde{\nabla}_0$ on w_b/u_*, approximately $\tilde{\nabla}_0 \propto (w_b/u_*)^2$ (Figure 14). For a given w_b/u_*, wave breaking reduces $\tilde{\nabla}_0$ by 1 order of magnitude relative to shear-driven boundary layer turbulence. Depending on wind and wave conditions, combined BW and LT effects reduce $\tilde{\nabla}_0$ by over 2 orders of magnitude.

5. Conclusions

In this first part of a two part investigation with focus on passive buoyant tracers in the ocean surface boundary layer (OSBL), we have examined the influence of equilibrium wind-waves on vertical tracer

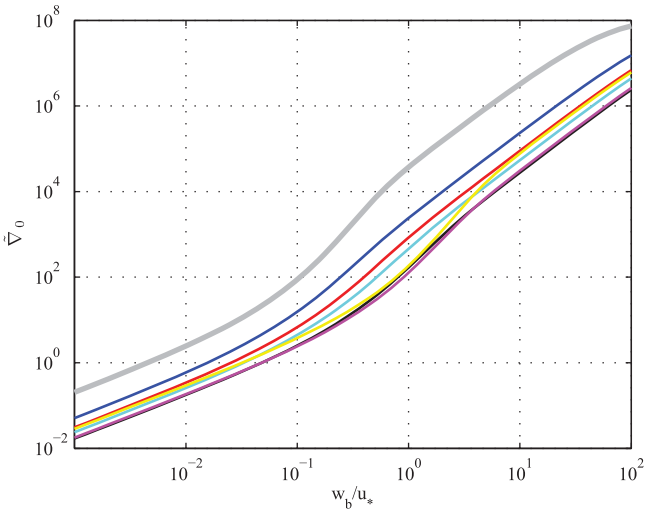

Figure 14. Normalized near-surface gradients (34) based on analytic solutions of (3) with (8) using the parameterizations (27) and (28) for $z_0 = 0.5$ m and $\lambda_p/h = 0.0$ (blue, BW only), 0.1 (red), 0.2 (cyan), 0.6 (black, e.g., $U_{10} = 5$ m/s, c_p/u_{*a}=35), 1.2 (magenta, e.g., $U_{10} = 7$ m/s, c_p/u_{*a}=35), 2.4 (yellow, e.g., $U_{10} = 10$ m/s, c_p/u_{*a}=35), and solutions without wave effects (gray).

distributions, based on large eddy simulations (LES) of the wave-averaged Navier-Stokes equation. The LES model captures both Langmuir turbulence (LT) and enhanced turbulent kinetic energy input due to breaking waves (BW). We impose a horizontally uniform breaking wave surface flux term that inputs TKE into the subgrid-scale motion. To impose wind-wave statistics in the equilibrium range, an empirical wave height spectrum is employed that depends only on water-side friction velocity u_* and a wave age c_p/u_*, where c_p is the peak phase speed. For a specified OSBL depth h, vertical concentration profiles of buoyant tracers are functions of four key parameters: w_b/u_*, c_p/u_*, λ_p/h, and z_0/h, where w_b symbolizes the buoyant rise velocity, λ_p is the peak wavelength, and z_0 denotes a hydrodynamic roughness length. In our approach, the wave age and peak wavelength are uniquely related to the turbulent Langmuir number and the Stokes drift decay depth, which are key parameters for Langmuir turbulence dynamics.

LES concentration profiles agree well with analytic solutions obtained for an eddy diffusivity profile that is constant near the surface and transitions into the K-Profile Parameterization (KPP) profile shape at greater depth. Without wave effects, LES results are consistent with solid-wall boundary layer KPP parameterizations. With wave effects, two KPP enhancement factors capture elevated wave mixing at a) greater depth (due to LT) and b) near-surface regions (due to both LT and BW). For smaller wave ages, BW critically enhances near-surface mixing, while LT effects are relatively small. For larger wave ages, both BW and LT contribute to elevated near-surface mixing and LT significantly increases turbulent transport at greater depth.

In our approach, the wave age can be expressed as turbulent Langmuir number, which is more commonly used to parameterize LT effects explicitly [e.g., *McWilliams and Sullivan*, 2000] and is related to the ratio of turbulent kinetic energy production due to Eulerian and Stokes drift shear [*McWilliams et al*., 1997; *Grant and Belcher*, 2009]. Being unambiguously determined from observed or modeled wave height spectra, the wave age seems appealing as a practical parameter for LT parameterizations. However, its correspondence to the short-wave distribution, and, thus, the Stokes drift vector is uncertain. In addition, our results indicate that LT parameterizations need to incorporate a nondimensional wave scale, e.g., λ_p/h, consistent with earlier findings [*Harcourt and D'Asaro*, 2008]. Physically, the turbulent kinetic energy production terms due to Eulerian and Stokes drift shear contain different shear length scales, whose ratio influences turbulence characteristics (see also discussion in *Kukulka et al*. [2013]).

Another important parameter for younger seas is the roughness length z_0, which is related to BW effects. In our approach, z_0 is imposed by the LES subgrid-scale model. In order to model z_0 due to BWs, an approach is needed that captures details of BW dynamics. The approach by *Sullivan et al*. [2007] provides an important framework for incorporating BW effects more realistically. In their current approach only a small fraction of the breaking wave energy transfer is resolved, which still needs to be assessed more systematically. Dissipative effects due to small-scale breaking wave motion on larger-scale coherent LT motions are determined by two nondimensional parameters λ_p/z_0 and La_t.

We have identified a range of realistic wind and wave conditions for which wave-driven turbulence is capable of deeply submerging buoyant tracers. For the range of $0.01 < w_b/u_* < 10$ detailed wind and wave conditions play the key role in the vertical distributions of buoyant tracers. For younger seas, BW effects are particularly important for near-surface distributions very close to the surface. Our results suggest that observations of deeply submerged buoyant tracers may provide an identifiable signature of wave-driven upper

ocean turbulence. For a given w_b/u_*, wave breaking reduces surface gradients of buoyant tracer concentrations by 1 order of magnitude relative to shear-driven boundary layer turbulence. Depending on wind and wave conditions, combined BW and LT effects reduce surface gradients by over 2 orders of magnitude.

This first part of the investigation provides a rational framework to systematically investigate observations of buoyant microplastic marine debris, which will be the focus of the second part of this investigation.

Appendix A

We examine some of the differences between the stochastic BW event model and the constant flux approach and investigate the role of various wave parameters. For simplicity, assume single-scale BWs with phase speed c, whose wavelength λ is governed by the linear dispersion relation. Consider an ocean surface area S large enough, so that for any given instance, the total breaking crest length is close to its expected value l and l/S is the BW distribution [*Phillips*, 1985]. The total force exerted by all BWs is $f_b = \tau S$ and the force exerted by a single event is Δf_b. Assume that Δf_b is homogeneously distributed over a cuboidal space-time volume with crest length Δl, depth Δz_b, along wave propagation extent Δx_b, and duration T_b. The energy transfer due to the breaking event force acting on the current is

$$\Delta E_b = \int_{T_b}\int_{V_b} \frac{\Delta f_b}{\Delta l \Delta x_b \Delta z_b} u(t,x,y,z)\, dV dt, \tag{A1}$$

where the integrations are over duration and the volume, V_b, of a breaker. The energy flux due to the resolved event force is then

$$F_{\text{events}} = \frac{1}{S T_b} \sum \Delta E_b, \tag{A2}$$

where the summation is over all $l/\Delta l$ instantaneous breaking events. If the turbulent currents are initially uncorrelated with BW event currents and its nonbreaking evolution time scale is much longer than T_b, we find for the total energy flux due to resolved events

$$F_{\text{events}} < \tau \frac{1}{\Delta z_b} \int_{-\Delta z_b}^{0} \langle u \rangle dz + \frac{\tau^2}{2\rho_w} \left(\frac{S}{l}\right) \frac{T_b}{\Delta x_b \Delta z_b}. \tag{A3}$$

The inequality is due to the assumption that all transferred energy is trapped in the same breaking volume for each event and its mass accelerated by Δf_b. The first right-hand-side term scales similar to stress-driven turbulence and converges to stress-driven turbulence for $\Delta z_b \to 0$. Note that the vertical extent of the breaking force may lead to a decrease of the total energy flux relative to stress-driven surface layers because the currents are larger closer to the surface. Also, the vertical extent decreases the shear to weaken shear instabilities. In fact, for large Δz_b the flow has characteristics of a pressure rather than stress-driven flow.

The second right-hand-side term is a result of BWs locally accelerating the currents to enhance the energy transfer because u locally increases. This term is larger for a longer duration and a spatially more concentrated local breaking force. To scale this term, one needs to estimate l/S. This can be accomplished by considering that the energy loss per unit time and unit crest length is [*Duncan*, 1981]

$$\epsilon_\Lambda = b \rho_w g^{-1} c^5, \tag{A4}$$

where b is a breaking strength coefficient in the range of 0.001–0.01, so that momentum constraints for linear surface waves imply $\tau S = l \epsilon_\Lambda c^{-1}$ from which l/S is readily determined. Furthermore, assume $\Delta x_b \sim \Delta z_b \sim \lambda$ and T_b is close to the BW period [*Sullivan et al.*, 2007], so that the second term becomes $b\tau g T_b/(8\pi^2)$. If we scale the first term as τu_*, the second term relative to the first one is $bgT_b/(8\pi^2 u_*)$. For the wave spectrum discussed above, we find $T_b \approx 0.3 T_p$, so that the last ratio is expressed as $0.3(4\pi)^{-1} b(c_p/u_*) \ll 1$. These scaling arguments suggest that the energy contribution due to the resolved stochastic events is relatively small in the *Sullivan et al.* [2007] approach, so that most BW energy transfer occurs on unresolved subgrid scales. Nevertheless, the *Sullivan et al.* [2007] approach captures locally enhanced SGS energy injection events and a long lived coherent breaking wave vortex [*Sullivan et al.*, 2004], whose impacts have yet to be systematically assessed on buoyant tracer distributions.

Acknowledgments
We would like to thank Fabrice Veron and Peter Sullivan for stimulating discussions and suggestions. Three anonymous reviewers provided constructive comments that have improved the manuscript. This work was supported by the U.S. National Science Foundation (grants OCE-1130678 and OCE-1352422) and NOAA Award NA10OAR4320148 Amendment 71. We acknowledge computational and staff resources from IT at the University of Delaware. The data for this paper are available from the author Tobias Kukulka (kukulka@udel.edu).

References

Colbo, K., and M. Li (1999), Parameterizing particle dispersion in Langmuir circulation, *J. Geophys. Res.*, *104*, 26,059–26,068.
Craig, P. D., and M. L. Banner (1994), Modeling wave-enhanced turbulence in the ocean surface layer, *J. Phys. Oceanogr.*, *24*(12), 2546–2559.
Craik, A. D. D., and S. Leibovich (1976), A rational model for Langmuir circulations, *J. Fluid Mech.*, *73*, 401–426.
D'Asaro, E. (2000), Simple suggestions for including vertical physics in oil spill models, *Spill Sci. Technol. Bull.*, *6*, 209–211.
D'Asaro, E. A. (2001), Turbulent vertical kinetic energy in the ocean mixed layer, *J. Phys. Oceanogr.*, *31*(12), 3530–3537.
D'Asaro, E. A., J. Thomson, A. Y. Shcherbina, R. R. Harcourt, M. F. Cronin, M. A. Hemer, and B. Fox-Kemper (2014), Quantifying upper ocean turbulence driven by surface waves, *Geophys. Res. Lett.*, *41*, 102–107, doi:10.1002/2013GL058193.
Denman, K. L., and A. E. Gargett (1995), Biological physical interactions in the upper ocean: The role of vertical and small-scale transport processes, *Annu. Rev. Fluid Mech.*, *27*, 225–255.
Donelan, M. A., J. Hamilton, and W. H. Hui (1985), Directional spectra of wind-generated waves, *Philos. Trans. R. Soc. London A*, *315*, 509–562.
Duncan, J. H. (1981), An experimental investigation of breaking waves produced by a towed hydrofoil, *Proc. R. Soc. London, Ser. A*, *377*(1770), 331–348, doi:10.1098/rspa.1981.0127.
Gargett, A. E., J. Wells, A. E. Tejada-Martinez, and C. E. Grosch (2004), Langmuir supercells: A mechanism for sediment resuspension and transport in shallow seas, *Science*, *306*, 1925–1928.
Gemmrich, J. (2012), Bubble-induced turbulence suppression in Langmuir circulation, *Geophys. Res. Lett.*, *39*, L10604, doi:10.1029/2012GL051691.
Gemmrich, J. R., and D. M. Farmer (1999), Near-surface turbulence and thermal structure in a wind-driven sea, *J. Phys. Oceanogr.*, *29*, 480–499, doi:10.1175/1520-0485(1999)029<0480:NSTATS>2.0.CO;2.
Gemmrich, J. R., and D. M. Farmer (2004), Near-surface turbulence in the presence of breaking waves, *J. Phys. Oceanogr.*, *34*, 1067–1086.
Gemmrich, J. R., M. L. Banner, and C. Garrett (2008), Spectrally resolved energy dissipation rate and momentum flux of breaking waves, *J. Phys. Oceanogr.*, *38*(6), 1296–1312.
Gerbi, G. P., J. H. Trowbridge, E. A. Terray, A. J. Plueddemann, and T. Kukulka (2009), Observations of turbulence in the ocean surface boundary layer: *Energetics and transport*, *39*(5), 1077–1096.
Grant, A. L. M., and S. E. Belcher (2009), Characteristics of Langmuir turbulence in the ocean mixed layer, *J. Phys. Oceanogr.*, *39*, 1871–1887.
Guha, A. (2008), Transport and deposition of particles in turbulent and laminar flow, *Annu. Rev. Fluid Mech.*, *40*(1), 311–341, doi:10.1146/annurev.fluid.40.111406.102220.
Harcourt, R. R., and E. A. D'Asaro (2008), Large eddy simulation of Langmuir turbulence in pure wind seas, *J. Phys. Oceanogr.*, *38*, 1542–1562.
Harcourt, R. R., and E. A. D'Asaro (2010), Measurement of vertical kinetic energy and vertical velocity skewness in oceanic boundary layers by imperfectly Lagrangian floats, *J. Atmos. Oceanic Technol.*, *27*, 1918–1935.
Huang, N. E. (1971), Derivation of stokes drift for a deep-water random gravity wave field, *Deep Sea Res. Oceanogr. Abstr.*, *18*(2), 255–259.
Komen, G. J., L. Cavaleri, M. Donelan, K. Hasselmann, S. Hasselmann, and P. A. E. M. Janssen (Eds.) (1996), *Dynamics and Modelling of Ocean Waves*, 1st ed., 532 pp., Cambridge Univ. Press, Cambridge, U. K.
Kukulka, T., and H. Hara (2005), Momentum flux budget analysis of wind-driven air-water interfaces, *J. Geophys. Res.*, *110*, C12020, doi:10.1029/2004JC002844.
Kukulka, T., and T. Hara (2008a), The effect of breaking waves on a coupled model of wind and ocean surface waves: I. Mature seas, *J. Phys. Oceanogr.*, *38*(10), 2145–2163.
Kukulka, T., and T. Hara (2008b), The effect of breaking waves on a coupled model of wind and ocean surface waves: II. Growing seas, *J. Phys. Oceanogr.*, *38*(10), 2164–2184.
Kukulka, T., T. Hara, and S. Belcher (2007), A model of the airsea momentum flux and breaking-wave distribution for strongly forced wind waves, *J. Phys. Oceanogr.*, *37*(7), 1811–1828.
Kukulka, T., A. J. Plueddemann, J. H. Trowbridge, and P. P. Sullivan (2009), Significance of Langmuir circulation in upper ocean mixing: Comparison of observations and simulations, *Geophys. Res. Lett.*, *36*, L10603, doi:10.1029/2009GL037620.
Kukulka, T., A. J. Plueddemann, J. H. Trowbridge, and P. P. Sullivan (2010), Rapid mixed layer deepening by the combination of Langmuir and shear instabilities: A case study, *J. Phys. Oceanogr.*, *40*(11), 2381–2400, doi:10.1175/2010JPO4403.1.
Kukulka, T., A. J. Plueddemann, J. H. Trowbridge, and P. P. Sullivan (2011), The influence of crosswind tidal currents on Langmuir circulation in a shallow ocean, *J. Geophys. Res.*, *116*, C08005, doi:10.1029/2011JC006971.
Kukulka, T., A. J. Plueddemann, and P. P. Sullivan (2012a), Nonlocal transport due to Langmuir circulation in a coastal ocean, *J. Geophys. Res.*, *117*, C12007, doi:10.1029/2012JC008340.
Kukulka, T., G. Proskurowski, S. Mort-Ferguson, D. W. Meyer, and K. L. Law (2012b), The effect of wind mixing on the vertical distribution of buoyant plastic debris, *Geophys. Res. Lett.*, *39*, L07601, doi:10.1029/2012GL051116.
Kukulka, T., A. J. Plueddemann, and P. P. Sullivan (2013), Inhibited upper ocean restratification in nonequilibrium swell conditions, *Geophys. Res. Lett.*, *40*, 3672–3676, doi:10.1002/grl.50708.
Langmuir, I. (1938), Surface motion of water induced by wind, *Science*, *87*, 119–123, doi:10.1126/science.87.2250.119.
Large, W., and S. Pond (1981), Open ocean momentum flux measurements in moderate to strong winds, *J. Phys. Oceanogr.*, *11*(3), 324–336.
Large, W., J. McWilliams, and S. Doney (1994), Ocean vertical mixing: A review and a model with a nonlocal boundary layer parameterization, *Rev. Geophys.*, *32*(4), 363–403.
Law, K. L., S. Mort-Ferguson, N. A. Maximenko, G. Proskurowski, E. E. Peacock, J. Hafner, and C. M. Reddy (2010), Plastic accumulation in the North Atlantic Subtropical gyre, *Science*, *329*(5996), 1185–1188, doi:10.1126/science.1192321.
Law, K. L., S. E. Mort-Ferguson, D. S. Goodwin, E. R. Zettler, E. DeForce, T. Kukulka, and G. Proskurowski (2014), Distribution of surface plastic debris in the eastern Pacific Ocean from an 11-year data set, *Environ. Sci. Technol.*, *48*(9), 4732–4738, doi:10.1021/es4053076.
Leibovich, S. (1983), The form and dynamics of Langmuir circulations, *Annu. Rev. Fluid Mech.*, *15*, 391–427.
Leibovich, S., and S. Paolucci (1981), The instability of the ocean to Langmuir circulations, *J. Fluid Mech.*, *102*, 141–167.
Li, M., and C. Garrett (1995), Is Langmuir circulation driven by surface waves or surface cooling?, *J. Phys. Oceanogr.*, *25*, 64–76, doi:10.1175/1520-0485(1995)025<0064:ILCDBS>2.0.CO;2.
Li, M., C. Garrett, and E. Skyllingstad (2005), A regime diagram for classifying turbulent large eddies in the upper ocean, *Deep Sea Res., Part I*, *52*(2), 259–278.
Li, M., S. Vagle, and D. M. Farmer (2009), Large eddy simulations of upper-ocean response to a midlatitude storm and comparison with observations, *J. Phys. Oceanogr.*, *39*, 2295–2309, doi:10.1175/2009JPO4165.1.

Li, S., M. Li, G. P. Gerbi, and J.-B. Song (2013), Roles of breaking waves and Langmuir circulation in the surface boundary layer of a coastal ocean, *J. Geophys. Res. Oceans*, *118*, 5173–5187, doi:10.1002/jgrc.20387.
Liang, J.-H., J. C. McWilliams, P. P. Sullivan, and B. Baschek (2011), Modeling bubbles and dissolved gases in the ocean, *J. Geophys. Res.*, *116*, C03015, doi:10.1029/2010JC006579.
McWilliams, J. C., and P. P. Sullivan (2000), Vertical mixing by Langmuir circulations, *Spill Sci. Technol. Bull.*, *6*, 225–2371.
McWilliams, J. C., P. P. Sullivan, and C. H. Moeng (1997), Langmuir turbulence in the ocean, *J. Fluid Mech.*, *334*, 1–30.
McWilliams, J. C., E. Huckle, J.-H. Liang, and P. P. Sullivan (2012), The wavy Ekman layer: Langmuir circulations, breaking waves, and Reynolds stress, *J. Phys. Oceanogr.*, *42*, 1793–1816.
Melville, W. K. (1996), The role of surface-wave breaking in air–sea interaction, *Annu. Rev. Fluid Mech.*, *28*, 279–321.
Melville, W. K., and P. Matusov (2002), Distribution of breaking waves at the ocean surface, *Nature*, *417*, 58–63, doi:10.1038/417058a.
Melville, W. K., F. Veron, and C. White (2002), The velocity field under breaking waves: Coherent structures and turbulence, *J. Fluid Mech.*, *454*, 203–233.
Moeng, C.-H. (1984), A large-eddy-simulation model for the study of planetary boundary–layer turbulence, *J. Atmos. Sci.*, *41*(13), 2052–2062.
Noh, Y., H. S. Min, and S. Raasch (2004), Large eddy simulation of the ocean mixed layer: The effects of wave breaking and Langmuir circulation, *J. Phys. Oceanogr.*, *34*(4), 720–735, doi:10.1175/1520-0485(2004)034<0720:LESOTO>2.0.CO;2.
Phillips, O. (1985), Spectral and statistical properties of the equilibrium range in wind-generated gravity waves, *J. Fluid Mech.*, *156*, 505–531.
Plant, W. J. (1982), A relationship between wind stress and wave slope, *J. Geophys. Res.*, *87*(C3), 1961–1967.
Plueddemann, A., J. Smith, D. Farmer, R. Weller, W. Crawford, R. Pinkel, S. Vagle, and A. Gnanadesikan (1996), Structure and variability of Langmuir circulation during the surface waves processes program, *J. Geophys. Res.*, *101*(C2), 3525–3543.
Polton, J. A., and S. E. Belcher (2007), Langmuir turbulence and deeply penetrating jets in an unstratified mixed layer, *J. Geophys. Res.*, *112*, C09020, doi:10.1029/2007JC004205.
Pope, S. B. (2008), *Turbulent Flows*, 5th ed., 771 pp., Cambridge Univ. Press, Cambridge, U. K.
Skyllingstad, E. (2003), The effects of Langmuir circulation on buoyant particles, in *Handbook of Scaling Methods in Aquatic Ecology: Measurement, Analysis, Simulation*, edited by P. G. Strutton and L. Seuront, pp. 445–457, CRC Press, Boca Raton, Fla., doi:10.1201/9780203489550.ch28.
Skyllingstad, E., and D. Denbo (1995), An ocean large-eddy simulation of Langmuir circulations and convection in the surface mixed layer, *J. Geophys. Res.*, *100*(C5), 8501–8522.
Skyllingstad, E. D., W. D. Smyth, J. Moun, and H. Wijesekera (1999), Upper-ocean turbulence during a westerly wind burst: A comparison of large-eddy simulation results and microstructure measurements, *J. Phys. Oceanogr.*, *29*(1), 5–28.
Smith, J. A. (1998), Evolution of Langmuir circulation during a storm, *J. Geophys. Res.*, *103*(C6), 12,649–12,668.
Smyth, W. D., E. D. Skyllingstad, G. B. Crawford, and H. Wijesekera (2002), Nonlocal fluxes and stokes drift effects in the K-profile parameterization, *Ocean Dyn.*, *52*, 104–115, doi:10.1007/s10236-002-0012-9.
Soloviev, A., and R. Lukas (2003), Observation of wave-enhanced turbulence in the near-surface layer of the ocean during {TOGA} {COARE}, *Deep Sea Res., Part I*, *50*(3), 371–395, doi:10.1016/S0967-0637(03)00004-9.
Sullivan, P. P., J. C. McWilliams, and W. K. Melville (2004), The oceanic boundary layer driven by wave breaking with stochastic variability. Part 1. Direct numerical simulations, *J. Fluid Mech.*, *507*, 143–174.
Sullivan, P. P., J. C. McWilliams, and W. K. Melville (2007), Surface gravity wave effects in the oceanic boundary layer: Large-eddy simulation with vortex force and stochastic breakers, *J. Fluid Mech.*, *593*, 405–452.
Terray, E., M. Donelan, Y. Agrawal, W. Drennan, K. Kahma, A. Williams, P. Hwang, and S. Kitaigorodskii (1996), Estimates of kinetic energy dissipation under breaking waves, *J. Phys. Oceanogr.*, *26*, 792–807.
Thorpe, S., T. Osborn, D. Farmer, and S. Vagel (2003), Bubble clouds and Langmuir circulation: Observations and models, *J. Phys. Oceanogr.*, *33*, 2013–2031.
Thorpe, S. A. (1982), On the clouds of bubbles formed by breaking wind-waves in deep water, and their role in air–sea gas transfer, *Philos. Trans. R. Soc. London A*, *304*(1483), 155–210.
Veron, F. (2015), Ocean spray, *Annu. Rev. Fluid Mech.*, *47*(1), 507–538, doi:10.1146/annurev-fluid-010814-014651.
Veron, F., and W. Melville (2001), Experiments on the stability and transition of wind-driven water surfaces, *J. Fluid Mech.*, *446*, 26–65.
Yang, D., M. Chamecki, and C. Meneveau (2014), Inhibition of oil plume dilution in Langmuir ocean circulation, *Geophys. Res. Lett.*, *41*, 1632–1638, doi:10.1002/2014GL059284.